Lawrence Berkeley National Laboratory
Recent Work

Title
THE CATEGORICAL SPACE OF FISSION Moretto, L.G

Permalink
https://escholarship.org/uc/item/93d7q1fs

Author
Wozniak, G.J. and

Publication Date
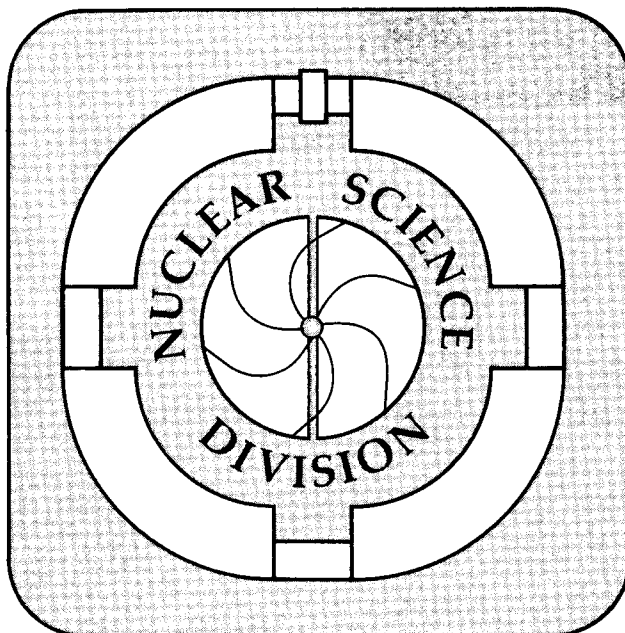1988-08-01

Lawrence Berkeley Laboratory
UNIVERSITY OF CALIFORNIA

Submitted to Pramana

DEC 5 1988

The Categorical Space of Fission

L.G. Moretto and G.J. Wozniak

August 1988

DISCLAIMER

The Categorical Space of Fission

LUCIANO G. MORETTO and GORDON J. WOZNIAK

Nuclear Science Division, Lawrence Berkeley Laboratory, University of California, Berkeley, California, 94720, USA

Abstract: The dualistic view of fission and evaporation as two distinct compound nucleus processes is substituted with a unified view in which fission, complex fragment emission and light particle evaporation are seen as part of a single process. The underlying connection between these decay modes is the mass asymmetry coordinate and the ridge line as the locus of the associated conditional barriers. The theoretical generalization is carried out explicitly. Complex fragment production at all mass asymmetries, throughout the periodic table, from low to intermediate bombarding energies is discussed in the light of compound nucleus decay.

1. Introduction

1.1 Early history and traditional views

To the deceptively simple question "What is fission?" the uncautious interviewer will obtain more of an answer than he bargained for. This is because fission has many shifting facets and corners and its definition changes with the space and time cross section of the scientists to whom the question is addressed.

Before 1939, fission was still in imaginary space. It emerged into an altogether too real world by virtue of two chemists who dared thinking the unthinkable. It was much more obvious to assume, as did Fermi, that the activities produced by neutrons on uranium were due to transuranium elements! So we can well imagine his surprise and mixed feelings when he realized he had been working with fission all along, much like Moliere's character who discovers with perplexity and a touch of awe that he has been speaking prose all of his life.

Even today a good number of our physics colleagues think of fission as a peculiar reaction occurring somewhere around uranium, a somewhat embarassing process that gave and still gives us a bad reputation; then with nuclear bombs, now with nuclear energy.

Even among "experts," fission is somehow associated with heavy elements. If its presence is acknowledged, as far down as the Lead region and even lower, its existence becomes progressively more evanescent as one moves farther down the periodic table and its cross section becomes lost in the abyss of nanobarns.

Most emphatically, fission is believed to be a unique kind of compound

nucleus reaction when compared with the more commonplace decays, like those involving the emission of protons, alphas and other "particles." A fission fragment is no "particle." It has nothing elementary about it and its emission suggests the involvement of collective degrees of freedom not associated with neutron decay. Furthermore, its high kinetic energy and its mass, both so far removed from those of an evaporated light particle seem to underscore the uniqueness of this process. Fission appeared so different from the other modes of compound nucleus decay that a separate theory was devised to calculate its decay width. As a result, we now have one theory for "evaporation" and another for fission.

Yet, a typical mass distribution of fission fragments while peaked, at times sharply, at masses near the symmetric splitting, is nonetheless a continuous distribution for which there are no firm boundaries other than those set by the total mass of the system. In all fairness, the search for ever lighter (and heavier) fission products was actively pursued by radiochemists, who were eventually stopped only by the abysmally small cross sections. So the belief was consolidated that fission fragments were confined to a rather narrow range of masses, despite the occasional disturbing detection of intermediate mass fragments like Na, Si, etc. in higher energy reactions (Alexander, 1963; Caretto, 1958; Friedlander, 1954,1963). With a curious twist of insight, these lighter fragments were at times attributed to ternary fission, rather than to a more obvious, highly asymmetric binary fission. After all, why should the fission mass distribution not extend all the way to alpha particles and protons?

1.2   The turbulent history of complex fragments

The advent of low energy heavy ions familiarized the nuclear community with products of deep inelastic reactions ranging throughout the periodic table (Schröder, 1977; Moretto, 1976, 1984). While, in many ways, deep inelastic reactions do remind us of fission, the obvious genetic relationship of these products with either target or projectile keeps these processes more or less within the categorical boundaries of "direct reactions."

Complex fragments made their grand entrance with intermediate-energy heavy ion reactions. In these processes, the elegant simplicity of quasi and deep inelastic processes is substituted by a glorious mess of products that seem to bear no relationship to either of the entrance channel partners. Their glaringly abundant production, together with the turbid experimental environment prevailing in early studies, prompted a tumultuous development of theories, claims and counterclaims about their origin and manner of production.

To the still untrained eye, such a complexity created irresistible images of new and exotic processes. For instance, the broad mass range and abundance of these fragments suggested mechanisms like the shattering of glass-like nuclei (Aichelin, 1984) or the condensation of droplets out of a saturated nuclear vapor (Fisher, 1967a, 1967b; Sauer, 1976; Finn, 1982; Bertsch, 1983; Siemens, 1983), or the somewhat equivalent picture of a nuclear soup curding simultaneously into many fragments. Such images were, and perhaps still are, so powerful that they thrived on themselves rather than

2

on experiment.

Fortunately, in spite of the confusion, it did not escape some perceptive members of our community that most, if not all of the complex fragments were associated with essentially binary processes. Furthermore, after an allowance was made for target and projectile-like fragments, the remaining fragments appeared to originate from the binary decay of an isotropic source. Finally, the excitation functions of these fragments appeared to behave in accordance with compound nucleus branching ratios. The inescapable conclusion was that compound nucleus decay was responsible for the production of these fragments by a mechanism able to feed all the possible asymmetries. The name that comes to mind as the most appropriate for this process is fission.

1.3 *Fission, fission everywhere.....*

This evidence, which continues to grow by the day, demonstrates the very pervasive presence of statistical complex fragment emission throughout the periodic table, at low and high excitation energies, covering the entire range of asymmetries, though not with equal intensity. In fact, the observed modulation of the mass distribution is a most revealing signature of the underlying potential energy as a function of mass asymmetry and underscores the essential unity of these processes.

Here one has the key for the unification of all compound nucleus decays into a single process. The natural connection between all these modes of decay is the mass asymmetry coordinate. Typical light particle evaporation (n, p, alpha, etc.) corresponds to very asymmetric decays, while "fission" of heavy systems corresponds to a very symmetric decay. The lack of emission at intermediate asymmetries is only apparent. Such an emission does in fact occur, albeit very rarely at low energies. The rarity of this occurrence is due to the important but accidental fact of the high potential barriers associated with the emission. A suitable increase of the excitation energy, or the lowering of the barriers by an increase in the angular momentum readily increases the cross section of these intermediate mass fragments to an easy level of detection.

Similarly the apparent lack of "fission" in lighter systems suggested by the absence of a symmetric fission peak in the mass distribution is another manifestation of the underlying potential energy that forces the mass distribution to assume a characteristic U shape. Consequently, in spite of the variety of mass distributions brought about by the different dependence of the potential energy on the mass asymmetry, we are confronted with a single process responsible for the production of the whole range of masses from the decay of compound nuclei throughout the periodic table (with the notable exception of gamma ray and meson emission). This process, with a minimal generalization of the term might well be called "fission."

In this way we have reached a very remarkable conclusion. Fission, rather than being a peculiar process relegated to the upper reaches of the periodic table and to a remote area of nuclear physics cultivated by oddball scientists, surprisingly turns out to be the most general, all-pervasive reaction in compound nucleus physics. If anything, it is the standard evaporation that

should be regarded as a peculiar limiting case of very asymmetric fission...
Like the ghost of Hamlet's father, fission is *hic et ubique* ," here, there and
everywhere.

In what follows, we are going to present first a generalized fission theory
which includes the mass asymmetry degree of freedom explicity; later we shall
present the experimental characterization of this process throughout the
periodic table, from energies a few MeV above the relevant barriers up to
bombarding energies of about 100 MeV/u.

2. General Fission Theory

As we have discussed above, the two canonical compound nucleus decay
channels recognized from the earliest times are particle evaporation and
fission. At very low energies the distinction between these two modes of
decay is quite apparent from an experimental point of view.

Particle evaporation traditionally includes neutron, proton and alpha
particle emission. Alpha emission did not appear strange despite the complex
nature of the particle because the lack of easily excited internal degrees of
freedom made ^{4}He look truly like an "elementary" particle. The similarity in
mass may have led to the incorporation of the somewhat rarer emissions of ^{2}H,
^{3}H, ^{3}He and other isotopes of He and Li under the "evaporation" label.

In its simplest form, the decay width is typically written down in terms of
the inverse cross section and of the phase space of the system with the
particle at infinity as:

$$\Gamma(\varepsilon)d\varepsilon = \frac{8\pi gm}{2\pi\rho(E)} \varepsilon \sigma(\varepsilon) \rho(E - B - \varepsilon)d\varepsilon \tag{1}$$

where $\rho(\varepsilon)$ and $\rho(E - B - \varepsilon)$ are the level densities of the compound nucleus and
residual nucleus, respectively; m, ε, g are mass, kinetic energy and spin
degeneracy of the emitted particle; and $\sigma(\varepsilon)$ is the inverse cross section
(Weisskopf, 1937, 1940, 1950, 1953).

On the other hand, fission involves the emission of fragments with
approximately one half the mass of the compound nucleus. The identification
of fission as an independent process is based upon the vast separation in
mass between the observable yields of fission fragments on one hand, and of
the evaporated particles (and evaporation residues) on the other.

The fission decay width is traditionally evaluated by following the
Bohr-Wheeler formalism which makes use of the transition-state method. In
this approach, the reaction (fission) coordinate is determined at a suitable
point in coordinate space, (typically at the saddle point) and the decay rate is
identified with the phase space flux across a hyperplane in phase space
passing through the saddle point and perpendicular to the fission direction.
The decay width is written (Wheeler, 1963) as:

4

$$\Gamma_f = \frac{1}{2\pi\rho(E)} \int \rho^*(E - B_f - \varepsilon)d\varepsilon, \qquad (2)$$

where $\rho(E)$ and $\rho^*(E - B_f - \varepsilon)$ are the level densities of the compound nucleus and of the saddle point; ε is the kinetic energy along the fission mode; and B_f is the fission barrier. So, the dichotomy between fission and evaporation is emphasized even in the expressions for the corresponding decay rates.

It was observed some time ago that this dichotomy is deceptive (Moretto, 1972b, 1975). The separation between evaporation and fission, it was claimed, was an optical illusion due to the very low cross section of products with masses intermediate between ^{4}He and fission fragments. If the emission of any fragment is not energetically forbidden, the mass distribution should be continuous from nucleons to symmetric products. Thus, there is no need to consider the two extremes of this distribution as two independent processes. **Rather, one would conclude, fission and evaporation are the two, particularly (but accidentally) obvious extremes of a single statistical decay process, the connection being provided in a very natural way by the mass asymmetry coordinate.**

As it turns out, it is indeed possible to bring out the yield of intermediate mass fragments from darkness, and experimental mass or charge yields from compound decay going continuously from ^{4}He to symmetry have now been obtained (Charity, 1988, 1988a, 1988b; Sobotka, 1984).

In order to demonstrate the inherent unity of fission and evaporation through complex fragment emission, it is useful to consider the potential-energy landscape as a function of a suitable set of collective coordinates, among which the mass asymmetry plays a dominant role.

2.1 The potential energy, absolute and conditional saddle points and ridge line

The potential-energy surface $V(\tilde{q})$ as a function of a set of deformation coordinates $\tilde{q}$ has been studied in detail first within the framework of the liquid-drop model (Cohen 1963, 1974; Nix, 1965), and, more recently of the finite-range model (Sierk, 1985, 1986). The liquid-drop model calculates the macroscopic nuclear energy for a given shape by evaluating the corresponding shape-dependent surface and Coulomb energies plus the volume and symmetry terms, which are shape independent. The finite-range model starts from a sharp-surface nucleus and spreads out the density by folding its shape with a Gaussian plus exponential function. In this way the diffuseness of the surface is dealt with, together with those proximity effects arising when portions of the nuclear surface happen to be close to each other as in strongly indented shapes.

The stationary points of the potential-energy surface, obtained by solving the set of equations

$$\frac{\partial V(\tilde{q})}{\partial \tilde{q}} = 0 \qquad\qquad (3)$$

comprise the ground state minimum and one to three saddle points, of which the saddle point with degree of instability one, if it exists, is known as the "fission" saddle point because of its relevance to the traditional fission process.

In general, only the points of the potential-energy surface corresponding to the solutions of the above equation are of intrinsic physical significance, because they are invariant under a canonical transformation of the coordinates. However, saddle-point shapes for fissility parameter values of $x < 0.7$ are strongly constricted at the neck, so that the nascent fission fragments are already well defined in mass and a physical significance to the mass asymmetry parameter $A_1/(A_1 + A_2)$ can be assigned. Then it is possible to consider a cut in the potential energy along the mass-asymmetry coordinate passing through the fission saddle point, with the property that at any point the potential energy is stationary with respect to all the other degrees of freedom. Each point is then a "conditional saddle point" with the constraint of a fixed mass asymmetry. This line has been called the "ridge line" (Moretto, 1972b, 1975) in analogy with the term "saddle point". The general shape of the ridge line depends on whether the fissility parameter lies above or below the Businaro-Gallone point (Businaro, 1955). This point corresponds to the fissility parameter value at which the symmetric saddle point gains/loses stability against the mass-asymmetry coordinate. For the liquid-drop model this point occurs at $x_{BG} = 0.396$ for zero angular momentum. The properties of the ridge line above and below the Businaro-Gallone point are illustrated in Fig. 1.

Below the Businaro-Gallone point, the ridge line shows a single maximum at symmetry. This is a saddle point of degree of instability two (the system is unstable both along the fission mode and the mass asymmetry mode). As the fissility parameter x increases above x_{BG}, this saddle point splits into three saddle points. The symmetric saddle point is stable with respect to the mass-asymmetry mode (degree of instability one) and is the ordinary fission saddle point. The other two saddles, of degree of instability two, are also called Businaro-Gallone mountains and flank symmetrically the fission saddle point. The incorporation of angular momentum maintains essentially the same topology. Its main effect is to decrease the overall heights of the barriers and to displace the Businaro-Gallone point towards lower values of the fissility parameter. This is illustrated in Fig. 2 where the finite-range barriers for the nucleus [110]Sn are plotted as a function of mass asymmetry (actually the atomic number Z of one of the fragments) and the angular momentum (Sobotka, 1987). At zero angular momentum the ridge line has a very flat maximum at symmetry, indicating that we are very near to the Businaro-Gallone point. As the angular momentum increases, one observes the development of a minimum at symmetry that becomes progressively deeper. This means that the system is moving above the Businaro-Gallone point with increasing angular momentum, or conversely that the Businaro-Gallone point occurs at progressively lower x values as the angular momentum increases.

Fig. 2 Two-dimensional plot of the asymmetry and angular-momentum dependent barriers for the decay of $^{110}Sn^*$ calculated with a finite-range model (Sobotka,1987).
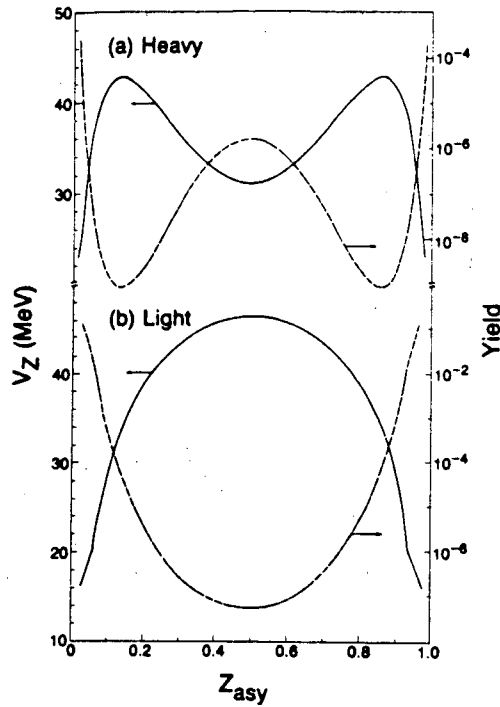

Fig. 1 Schematic ridge-line potentials (solid curve) and expected yields (dashed curve) for: a) a heavy CN above the Businaro-Gallone point; and b) a light CN below the Businaro-Gallone point as a function of the mass asymmetry coordinate (Z_{asy}). See Eq. 13 in the text.
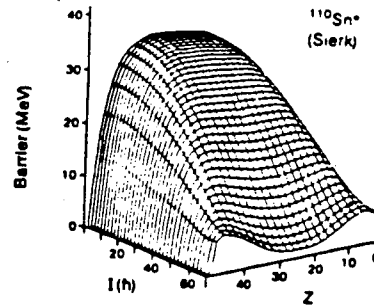
2.2 Complex fragment radioactivity as a very asymmetric spontaneous fission decay.

The explicit introduction of the mass-asymmetry coordinate in the problem of complex fragment emission, resulting in the ridge line as a generalization of the fission saddle point, leads, as a first application, to the theory of complex fragment radioactivity. Let us consider the qualitative picture in Fig. 3 where the potential energy is shown as a function of the mass asymmetry coordinate as well as of the fission coordinate (decay coordinate). The ridge line divides the compound nucleus domain from the fission-fragment domain. A continuum of trajectories is available now for the decay, from the easy path through the saddle point, to the very arduous path reaching up to the Businaro-Gallone mountains, and down to the progressively easier paths of more and more asymmetric decays, eventually leading to α particle and nucleon decay.

7

For spontaneous decay we can associate each path with the action integral:

$$S(Z) = \int |p(x)|dx = \int_a^b [2\mu(Z)\, V(Z,x)]^{1/2}dx \qquad (4)$$

where $|p(x)|$ is the modulus of the momentum along the fission coordinate x; $\mu(Z)$ and $V(Z,x)$ are the inertia and the potential energy for each asymmetry Z; and **a** and **b** are the classical turning points of the trajectory. The decay rate $P(Z)$ can be written, semiclassically, as

$$P(Z) = w(Z)\, \exp\left[\frac{-2S(Z)}{\hbar}\right] \qquad (5)$$

where $w(Z)$ is the frequency of assault of the barrier for the asymmetry Z.

This simple expression accomodates the radioactive emission of any fragment, provided that the process is energetically possible. Of course the strong dependence of the decay rate on the barrier height tends to favor the emission of very light particles on the one hand, and, for very heavy elements, spontaneous fission decay. For light particle emission, shell effects play a dominant role. The strong magicity of ^{4}He accounts for the very pervasive α radioactive decay. The recently observed (Barwick, 1986; Gales, 1984; Price, 1985; Rose, 1984) radioactive emission of ^{14}C and ^{24}Ne can be accounted for in a very similar way by the very strong shell corrections associated with the residual nuclei in the ^{208}Pb region. Extensive discussions of this problem can be found in Poenaru (1985) and Shi (1985a, 1985b).
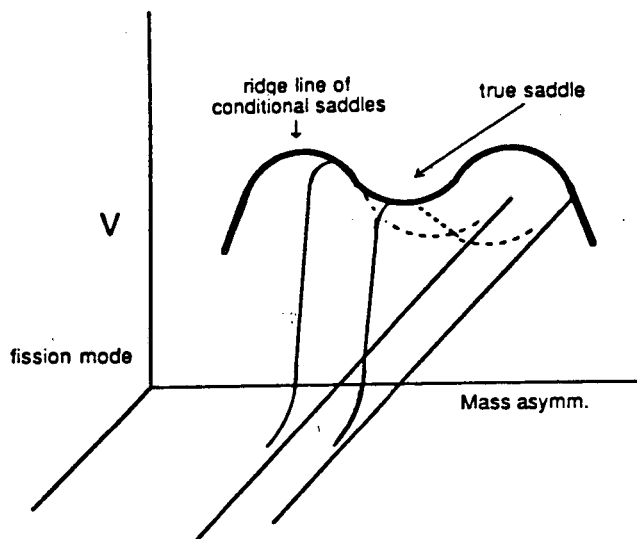

Fig. 3 Schematic potential energy surface as a function of the reaction coordinate and of the mass-asymmetry coordinate.

2.3 Complex fragment decay width

The role of the ridge line on the emission of complex fragments can be appreciated by observing that for x < 0.7 at all asymmetries and for x > 0.7 over a progressively reduced range of asymmetries, the nuclear shapes at the ridge line are so profoundly necked-in that ridge and scission lines approximately coincide. This means that, as the system reaches a given point on the ridge line, it is, to a large extent, committed to decay with the corresponding saddle asymmetry. On the basis of the transition-state theory one can write, for the partial decay width (Moretto, 1975):

$$\Gamma(Z)dZ = \frac{dZ}{2\pi\rho(E)} \int \rho^{**}[E - B(Z) - \varepsilon]d\varepsilon \qquad (6)$$

where $\rho(E)$ is the compound nucleus level density, and $\rho_{**}[E - B(Z) - \varepsilon]$ is the level density at the conditional saddle of energy $B(Z)$, which the system is transiting with kinetic energy ε.

The units and the number of degrees of freedom associated with the various level densities are clarified by the following relations :

$$\Gamma_Z(Z)dZ = \frac{dZ}{2\pi\rho(E)} \int \rho^{**}[E-B(Z)-\varepsilon]d\varepsilon \cong \frac{1}{2\pi\rho(E)}\rho^{**}[E-B(Z)]\int e^{-\varepsilon/T}d\varepsilon \cong \frac{T}{2\pi\rho(E)}\rho^{**}[E-B(Z)]. \quad (7)$$

Well above the Businaro-Gallone point, one can expand the potential energy as:

$$B(Z) = B_F + bZ^2. \qquad (8)$$

This gives rise to a fission peak whose integrated yield is:

$$\Gamma_F \cong \frac{T\rho^{**}(E-B_F)}{2\pi\rho(E)}\int e^{-bZ^2/T} dZ = \frac{T^{3/2}\pi^{1/2}}{2\pi\rho(E)b^{1/2}}\rho^{**}(E-B_F) = \frac{T}{2\pi\rho(E)}\rho^*(E-B_F) \quad (9)$$

where we have set

$$\sqrt{\frac{\pi T}{b}}\rho^{**}(E-B_F) = \rho^*(E-B_F). \qquad (10)$$

Alternatively,

$$\Gamma_F = \frac{1}{2\pi\rho(E)}\int \rho^{**}(E-B_F-bZ^2-\varepsilon)dZd\varepsilon = \frac{1}{2\pi\rho(E)}\sqrt{\frac{\pi T}{b}}\int \rho^{**}(E-B_F-\varepsilon)d\varepsilon \quad (11)$$

9

$$= \frac{T}{2\pi\rho(E)} \sqrt{\frac{\pi T}{b}} \rho^{**}(E - B_F) = \frac{T}{2\pi\rho(E)} \rho^*(E - B_F) . \tag{12}$$

These results allow us to make qualitative predictions on the shape of the mass/charge distributions. Equation 7 can be further simplified as follows:

$$\Gamma_Z \propto \frac{\rho^{**}[E - B(Z)]}{\rho(E)} \propto e^{-B(Z)/T_Z} \tag{13}$$

where T_Z represents the nuclear temperature calculated at an excitation energy

$$E_x = E - B(Z) = aT_Z^2 . \tag{14}$$

This means that the mass or charge yield mirrors the ridge line, being characterized by high emission probabilities in the regions of low potential energy and vice-versa. This is illustrated in Fig. 1 for two systems, one below the Businaro-Gallone point and the second above it. In the former case the yield has a characteristic U shape, where the light wing is associated with very light particle emission and the complementary heavy wing with the corresponding evaporation residues. In the latter case, besides the light and heavy wings observed in the former case, one observes also a peak at symmetry which becomes more and more prominent with increasing fissility parameter x and which can be identified as the fission peak.

In the limit in which the conditional saddle and scission points can be considered degenerate, one can develop also a theory of the complex fragment kinetic energy and angular distributions.

2.4 A transition state formalism for thermal spectra

In the case of neutron emission, the kinetic energy spectra can be easily calculated, since the velocity of the system at the conditional saddle corresponds closely to the velocity of the neutron at infinity. This is not quite the case for the emission of a charged complex fragment for which the kinetic energy at infinity comes from a variety of sources. Besides the velocity along the decay coordinate, one must also consider the potential and kinetic energies associated with other modes, but which end up nonetheless as translational kinetic energy of the fragment at infinity. It is not difficult to develop a formalism that takes into account some of these effects in a statistically consistent way.

We can write down the complex fragment decay rate in terms of the normal modes about a "saddle point" in a suitable deformation space (Moretto, 1972b, 1975). This saddle point could be searched, for instance, among the shapes corresponding to the complex particle in near contact with the surface of the residual nucleus, which in turn can assume a variety of deformations.

It is helpful to consider a sphere-spheroid model where the smaller

spherical fragment is in contact with a larger spheroidal fragment of variable eccentricity. The relevant collective degrees of freedom can be catalogued as shown in Fig. 4 in the framework of the sphere-spheroid model.
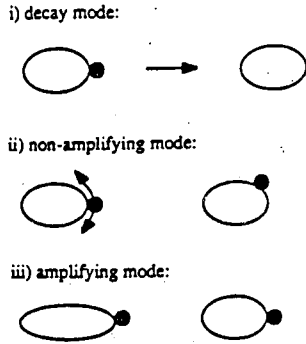
i) decay mode:

ii) non-amplifying mode:

iii) amplifying mode:

Fig. 4 Schematic representation of the three kinds of normal modes at the conditional saddle point, which control the kinetic energy at infinity.
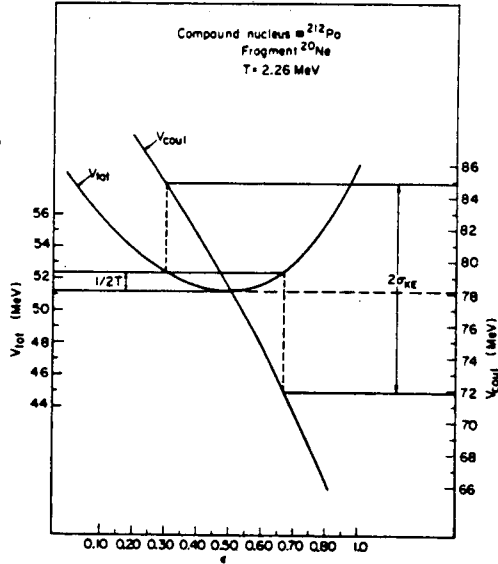
Compound nucleus = ^{212}Po
Fragment ^{20}Ne
T = 2.26 MeV

V_{coul}

V_{tot}

$1/2T$

$2\sigma_{KE}$

V_{tot} (MeV)

V_{coul} (MeV)

0.10 0.20 0.30 0.40 0.50 0.60 0.70 0.80 1.0

Fig. 5 Potential energy and Coulomb interaction energy as a function of the deformation of the large fragment (sphere-spheroid model). The thermal fluctuations about the ridge point result in larger amplified fluctuations in the Coulomb repulsion energy (Moretto, 1975).

The first class corresponds to the decay mode, which is unbound and analogous to the fission mode.

The second class includes the non-amplifying modes whose excitation energy is directly translated into kinetic energy at infinity without amplification. Two such modes could be, for instance, the two orthogonal oscillations of the particle about the tip of the "spheroidal" residual nucleus. With these two modes, the particle can experience the whole distribution of Coulomb energies associated with a given deformation of the residual nucleus.

The third class corresponds to the amplifying modes. In these modes the total potential energy remains rather flat about the minimum, while complementary substantial changes occur in the Coulomb and surface energies. As shown in Fig. 5, an oscillation about this mode involving an amount of energy on the order of the temperature corresponds to a variation in the monopole - monopole term of the Coulomb energy

$$\Delta E_C = 2\sqrt{\frac{c^2 T}{k}} = 2\sqrt{pT} \qquad (15)$$

11

where the coefficients c and k are defined by the quadratic expansion of the total potential energy associated with the deformation mode z:

$$V(z) = B_0 + kz^2 \tag{16}$$

and by the linearization of the Coulomb energy along the same mode:

$$E_{Coul} = E^0_{Coul} - cz. \tag{17}$$

The quantities B_0, E^0_{Coul}, c, k and p are defined at the minimum of the total potential energy with respect to the deformation mode, and are, as a consequence, saddle-point quantities. Because of its effect, illustrated in Fig. 5, p is called the "amplification parameter". An input thermal noise of the order of the temperature T is magnified in accordance to Eq. 15 and Fig. 5 giving an output kinetic energy fluctuation much greater than the temperature. This effect is probably responsible also for the great widths of the kinetic energy distributions in ordinary fission.

After having identified and classified the normal modes at the saddle point, one can write down the decay width as:

$$\Gamma^n d\varepsilon \, \Pi \, dx_i \, dp_i = \frac{1}{2\pi\rho(E)} \rho^{**} \left[E - B_0 - \varepsilon - \sum \left(a_i x_i^2 + \frac{p_i^2}{2m_i} \right) \right] d\varepsilon \, \Pi \left[\frac{dx_i \, dp_i}{h} \right] \tag{18}$$

where ε is the kinetic energy along the decay mode and a_i, m_i are the stiffnesses and the inertias of the bound modes.

With excellent accuracy one can expand $\ln \rho^{**}$ to obtain:

$$\Gamma^n d\varepsilon \, \Pi \, dx_i dp_i = \frac{\rho^{**}(E - B_0)}{2\pi\rho(E)} \exp\left[-\frac{1}{T} \left[\varepsilon + \sum \left(a_i x_i^2 + \frac{p_i^2}{2m_i} \right) \right] \right] d\varepsilon \, \Pi \left[\frac{dx_i dp_i}{h} \right] \tag{19}$$

where the saddle temperature T is given by:

$$\frac{1}{T} = \frac{d \ln \rho^{**}(x)}{dx} \bigg|_{x = E - B_0}. \tag{20}$$

We are now going to consider three specific cases. The first and simplest deals in detail with only one decay mode and one amplifying mode. The decay width becomes:

$$\Gamma(\varepsilon, z) \, d\varepsilon dz \propto e^{-(\varepsilon + kz^2)/T} \, d\varepsilon dz. \tag{21}$$

Remembering that the final kinetic energy can be written as:

$$E = E^0_{Coul} - cz + \varepsilon \tag{22}$$

we can rewrite the decay width as follows:

12

$$\Gamma(\varepsilon,z) \;\propto\; \exp\left[-\frac{\varepsilon + (E - E^0_{Coul} - \varepsilon)^2/p}{T}\right] \tag{23}$$

or

$$\Gamma(\varepsilon,z) \;\propto\; \exp\left[-\frac{\varepsilon + (x - \varepsilon)^2/p}{T}\right], \tag{24}$$

where $x = E - E^0_{Coul}$.

The final kinetic energy distribution is obtained by integrating over ε:

$$P(E) \;\propto\; \int \exp\left[-\frac{\varepsilon + (x - \varepsilon)^2/p}{T}\right] d\varepsilon \tag{25}$$

or

$$P(E) = 1/2\,(\pi p T)^{1/2}\, e^{\frac{p}{4T}}\, e^{-\frac{x}{T}} \left\{ \mathrm{erf}\left[\frac{2E^0_{Coul} + p}{2(pT)^{1/2}}\right] - \mathrm{erf}\left[\frac{p - 2x}{2(pT)^{1/2}}\right] \right\}. \tag{26}$$

This formula elegantly allows for the following features:
1) The particle is emitted from the deformed saddle point configuration.
2) Shape fluctuations with the associated Coulomb fluctuations are accounted for in a statistically consistent way.

The addition of two harmonic non-amplifying modes (potential energy only) like those illustrated in Fig. 4 or of one non-amplifying mode (potential + kinetic energy) leads to a more general expression

$$\Gamma(\varepsilon,z) \;\propto\; \varepsilon\left[\exp\left[-\frac{\varepsilon + (x - \varepsilon)^2/p}{T}\right]\right] \tag{27}$$

which, after integration over ε gives:

$$P(E) = \frac{(\pi p T)^{1/2}}{2} e^{\frac{p}{4T}} e^{-\frac{x}{T}} \left[\frac{2x - p}{2}\left\{ \mathrm{erf}\left[\frac{2E^0 + p}{2(pT)^{1/2}}\right] - \mathrm{erf}\left[\frac{p - 2x}{2(pT)^{1/2}}\right] \right\} - \left(\frac{pT}{\pi}\right)^{1/2}\left\{ \exp\left[-\frac{(2E^0 + p)^2}{4pT}\right] - \exp\left[-\frac{(p - 2x)^2}{4pT}\right] \right\} \right]. \tag{28}$$

This formula not only portrays the same features as that derived previously, but also allows for emission of the particle from any point of the

surface (if the Coulomb potential is assumed to vary quadratically as the particle moves away from the pole toward the equator of the residual nucleus). It is not unexpected but interesting to notice that Eq. 28 does not depend on any parameter associated with the potential or kinetic energy of the non-amplifying modes but depends only on their number. In this way the problem of the integration over the Coulomb field at the nuclear surface is elegantly bypassed.

One can extend the derivation of these equations to a greater number of non amplifying modes, as shown by Moretto (1975). The general shapes predicted by these equations depend on the parameter p which is essentially a surface-Coulomb parameter. At small values of p corresponding to the emission of small particles, the distributions are skewed and Maxwellian-like, while at larger values of p, corresponding to the emission of sizeable fragments, the distributions become Gaussians. This is illustrated in Figs. 6a & b, where the kinetic energy distributions assuming 0,1,2 non amplifying modes are calculated at various temperatures for the emission of an α particle (small p) and a carbon ion (large p) from a ^{212}Po compound nucleus.

In the limit of large p, these equations become of the form $p(x) \cong \exp[-x^2/pT]$, which reminds us of the Gaussian kinetic energy distributions
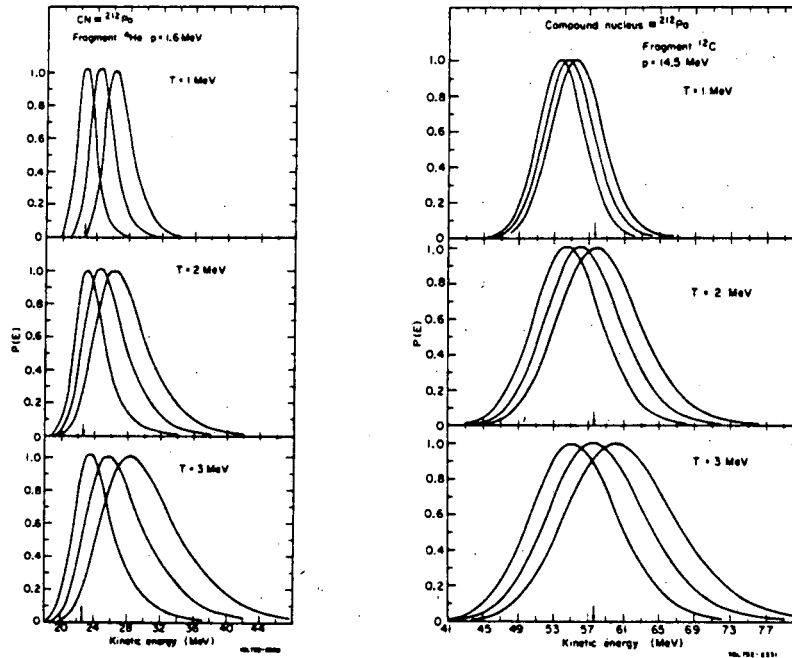
Fig. 6   Calculated kinetic energy distributions at three temperatures for small [(a) α particles] and large [(b)^{12}C fragments] values of the amplification parameter p for the decay of a ^{212}Po nucleus. The curves corresponding to 0,1,2 non amplifying modes can be identified by their progressive shift towards higher kinetic energies. The arrows indicate the energies corresponding to the ridge line Coulomb energies (Moretto, 1975).

14

observed in ordinary fission. Another pleasing feature of these equations is the limit to which they tend for p=0:

$$P(E) \propto e^{-E/T} \qquad \text{and} \qquad P(E) \propto E\, e^{-E/T}. \qquad (29)$$

Therefore the evolution of the kinetic energy spectra from Maxwellian-like to Gaussian-like as one goes from "evaporation" to "fission" is naturally predicted in this model. The latter form is the standard "evaporation" expression for the neutron spectra.

To summarize, we have calculated analytical expressions for the kinetic energy distributions which need only the following parameters to be extracted from any suitable model.

1) The monopole-monopole Coulomb energy E^0 of the relevant saddle shape.
2) The amplification parameter p.
3) The number of non-amplifying modes.

2.5 Angular distributions

Continuing the generalization of the fission process, the angular distributions for the emitted particles can also be derived. The ridge-point configuration, for the great majority of cases, can be identified with the scission configuration. Furthermore, the disintegration axis and the symmetry axis of the system at the ridge point should approximately coincide. As a consequence, the projection K of the total angular momentum I on the symmetry/disintegration axis should remain constant from the ridge point to infinity. Such a condition implies a relationship between the total angular momentum and the orbital angular momentum of the two fragments, thus determining the final angular distribution. In fission theory, the assumption of constant K from saddle to infinity is somewhat uncertain, especially for very heavy elements, due to the complicated dynamical evolution leading from saddle to scission. In the present case, the closeness of the ridge and the scission points should make the theory work even better than in fission.

The differential cross section can be written as follows (Moretto, 1975):

$$\frac{d\sigma}{d\Omega} = \int_0^{I_{max}} dI\, \sigma_I \int_{-I}^{+I} dK\, \frac{\Gamma_f^I (K)}{\Gamma_T^I}\, W_K^I (\theta)\,, \qquad (30)$$

where

$$\Gamma_f^I (K) = \frac{\Gamma_f^0}{2I+1}\, \exp\left[-\frac{\hbar^2 I^2}{2T} (\mathfrak{I}_\perp^{-1} - \mathfrak{I}_c^{-1}) \right] \exp\left[-\frac{K^2}{2K_0^2} \right]. \qquad (31)$$

Here σ_I is the reaction cross section for the I-th partial wave, and $W_K^I (\theta)$ can be written in the classical limit as:

15

$$W_K^I(\theta) \propto \frac{2I + 1}{\sqrt{\sin^2\theta - \dfrac{K^2}{I^2}}} \ . \tag{32}$$

In Eq. 31, $\Im_c$ is the compound nucleus moment of inertia; K^2_0 is the standard deviation of the statistical distribution of K-values and is given by:

$$K_0^2 = \Im_{\text{eff}} \, T/\hbar^2 \ . \tag{33}$$

The quantity $\Im_{\text{eff}}$ is related to the principal moments of inertia, $\Im_{\parallel}$ and $\Im_{\perp}$, of the system at the ridge point by the relation:

$$\frac{1}{\Im_{\text{eff}}} = \frac{1}{\Im_{\parallel}} - \frac{1}{\Im_{\perp}} \ . \tag{34}$$

It is worth considering that, at fixed temperature T, the width of the K-distribution becomes broader as the ridge configuration becomes more compact.

If one assumes that $\Gamma_T \approx \Gamma_n$, the integration over K of Eq. 30 gives:

$$W(\theta) \propto \int_0^{I_{\text{max}}} \frac{2I dI \exp\left[-\dfrac{I^2 \sin^2\theta}{4K_0^2}\right] I_0\left[\dfrac{I^2 \sin^2\theta}{4K_0^2}\right]}{\exp(-\beta I^2)} \ . \tag{35}$$

In this expression I_0 is the modified Bessel function of order 0 and

$$\beta = \frac{\hbar^2}{2T}\left[\frac{1}{\Im_n} - \frac{1}{\Im_{\perp}}\right] \ , \tag{36}$$

$\Im_n$ being the moment of inertia of the residual nucleus after neutron emission. If $\beta I^2 \ll 1$ then $\exp(-\beta I^2) \approx 1$ and the integral becomes of the form:

$$W(\theta) \propto \frac{1}{\sin^2\theta} \int_0^{s_{\text{max}}} \exp(-s) I_0(s) ds = \frac{s_{\text{max}}}{\sin^2\theta} \exp(-s_{\text{max}})\left[I_0(s_{\text{max}}) + I_1(s_{\text{max}})\right], \tag{37}$$

where $s = I^2 \sin^2\theta/4K^2_0$, $s_{\text{max}} = I^2_{\text{max}} \sin^2\theta/4K^2_0$, and I_0, I_1 are the modified Bessel functions of order 0, 1. Explicitly, one obtains:

$$W(\theta) \propto \exp\left[-\frac{I_{max}^2 \sin^2\theta}{4K_0^2}\right]\left\{I_0\left[\frac{I_{max}^2 \sin^2\theta}{4K_0^2}\right]+I_1\left[\frac{I_{max}^2 \sin^2\theta}{4K_0^2}\right]\right\} \quad . \quad (38)$$

In order to obtain a better accuracy one can expand the denominator to higher order:

$$e^{\beta I^2} \sim 1 + \beta I^2 \quad . \quad (39)$$

In many cases, for large temperatures, such an expansion ought to be adequate even at rather large angular momenta. Then the angular distribution becomes:

$$W(\theta) \propto \exp(-s_{max})\left[I_0(s_{max})+I_1(s_{max})\right]+\frac{\beta I_{max}^2}{2}\exp(-s_{max})\left[I_0(s_{max})+\frac{2I_1(s_{max})}{3}-\frac{I_2(s_{max})}{3}\right]. \quad (40)$$

This expression has two interesting limits: as $g = I_{max}^2/4K_0^2$ tends to infinity (either because K_0^2 tends to zero or because I_{max} becomes very large), one can use the asymptotic expression for the Bessel functions:

$$I_\nu(s) = \frac{e^s}{\sqrt{2\pi s}}\left[1-\frac{4\nu^2-1}{8s}+\ldots\right] \quad . \quad (41)$$

Then if ones keeps only the lowest term in the $s^{-1/2}$ expansion one obtains:

$$\lim_{g\to\infty} \quad W(\theta) \propto \frac{1}{\sin\theta} \quad . \quad (42)$$

On the other hand, as $g \to 0$ (either because $I_{max} \approx 0$ or $K_0^2 \to \infty$) one obtains:

$$\lim_{g\to 0} \quad W(\theta) = \text{constant} \quad . \quad (43)$$

These limits represent the two extreme cases for the coupling between total and orbital angular momentum. The coupling is maximum in the first case and zero in the second case. The coupling parameter g depends upon the principal moments of inertial of the ridge configuration. This allows one to make a very simple prediction. At constant I_{max}, g becomes larger the bigger the difference between $\mathcal{S}_\parallel$ and $\mathcal{S}_\perp$, or in other words, the more elongated the ridge configuration is. Thus the anisotropy $W(0^\circ)/W(90^\circ)$ progressively increases as one considers the emission of a neutron, an α-particle, a lithium particle, a beryllium particle, etc. (see Fig. 7). It is amusing to note that Eq. 40 gives reasonable predictions for the angular distribution of neutrons as well. The ridge-point configuration for neutron emission is represented by a neutron just outside the nucleus. The principal moments of inertia can be approximately expressed as follows:

$$\mathfrak{I}_{\parallel} \approx \mathfrak{I}, \qquad \mathfrak{I}_{\perp} \approx \mathfrak{I} + \mu R^2, \tag{44}$$

where $\mathfrak{I}$ is the moment of inertia of the residual nucleus, μ is the reduced mass of the neutron-nucleus system and R is the distance between the neutron and the nucleus when they are in contact. In many cases $\mathfrak{I} \gg \mu R^2$. Thus the quantity s takes the approximate form:

$$s = \frac{\hbar^2 \, l_{max}^2 \sin^2\theta}{4T} \left[\frac{1}{\mathfrak{I}_{\parallel}} - \frac{1}{\mathfrak{I}_{\perp}} \right] \approx \frac{\hbar^2 \, l_{max}^2 \sin^2\theta}{4T\mathfrak{I}} \left[1 - \frac{1}{1 + \mu R^2/\mathfrak{I}} \right]$$

$$\approx \frac{\hbar^2 \, l_{max}^2 \sin^2\theta}{4T\,\mathfrak{I}} \frac{\mu R^2}{\mathfrak{I}} = \frac{\langle E_R \rangle}{T} \frac{\mu R^2}{\mathfrak{I}} \sin^2\theta, \tag{45}$$

where $\langle E_R \rangle$ is the mean rotational energy of the residual nucleus. Similarly,

$$\mathfrak{I}_c \approx \mathfrak{I}_{\parallel} \approx \mathfrak{I}, \qquad \frac{1}{2}\beta \, l^2 = \frac{s}{\sin^2\theta} = \frac{\langle E_R \rangle}{T} \frac{\mu R^2}{\mathfrak{I}} = \alpha. \tag{46}$$
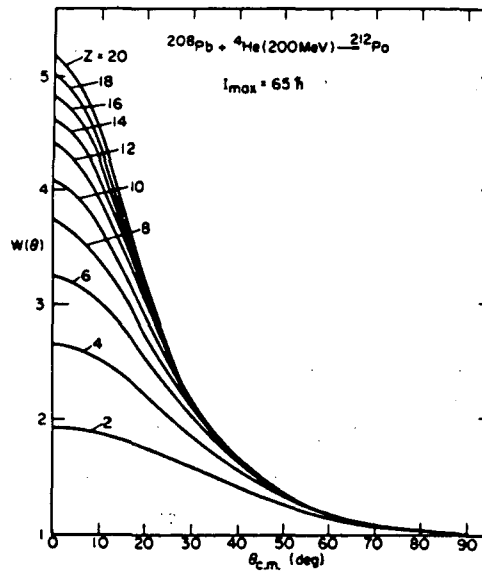
Fig. 7 Calculated angular distributions of various fragments emitted by the compound nucleus formed in the reaction ^{208}Pb + 200 MeV ^{4}He $\rightarrow$ [^{212}Po*] $\rightarrow$ Z + (84 - Z). Note the progressive approach to a 1/sin θ distribution with increasing atomic number of the fragments (Moretto, 1975).

18

Expanding Eq. 40 to first order in s we obtain:

$$W(\theta) \approx 1 - \frac{s}{2} + \frac{\beta I_{max}^2}{2}\left[1 - \frac{2s}{3}\right] = 1 + \frac{<E_R>}{T}\frac{\mu R^2}{3} - \frac{<E_R>}{2T}\frac{\mu R^2}{3}\sin^2\theta$$

$$= 1 + \alpha - \frac{1}{2}\alpha \sin^2\theta .$$

(47)

The normalized angular distribution in first order takes the form:

$$\frac{W(\theta)}{W(90)} = 1 + \frac{1}{2}\alpha \cos^2\theta = 1 + \frac{1}{2}\frac{<E_R>}{T}\frac{\mu R^2}{3}\cos^2\theta .$$

(48)

The same normalized distribution has been obtained by Ericson (1960) from a more conventional evaporation theory.

3. Experimental Evidence For Statistical Binary Decay

3.1 Compound nucleus emission at low energies

In the midst of a confusing experimental situation at intermediate energies, made even less clear by a variety of theoretical claims and counterclaims, a descent to lower energies helped to clarify at least one point, namely the compound nucleus emission of complex fragments. The reaction chosen for this purpose, ^{3}He + Ag, presented several advantages (McMahan, 1985; Sobotka, 1983). On the one hand, the very lightness of the projectile eliminated a source of complex fragments otherwise present with heavier projectiles, namely projectile fragmentation. On the other hand, the reaction Q-value helped to introduce a good amount of excitation energy with a moderate bombarding energy.

The excitation energy of the compound nucleus ranged from 50 MeV to 130 MeV, the lower limit being barely 10 MeV above the highest barriers. Complex fragments were detected with cross sections dropping precipitously with decreasing energy. Their kinetic energy specta resembled closely the shapes predicted by the theory illustrated above. In particular, the shapes evolved from Maxwellian-like for the lowest Z values to Gaussian-like for the highest Z values.

A very effective way to appreciate the nature of the emission and the possible source of these fragments is to plot their invariant cross section in velocity space. The invariant cross section plots in the $v_{\parallel}$ - $v_{\perp}$ plane shown in Fig. 8 for a variety of fragments at 70 MeV bombarding energy demonstrate striking Coulomb rings which are the paradigms of many more to follow in the next pages. The essentially binary nature of the decay, its angular isotropy, and the extent of energy relaxation speak suggestively of compound nucleus decay. However, the crucial proof is given by the measurement of excitation functions extending down almost to the threshold. These excitation functions, shown in Fig. 9 are very similar to the fission excitation functions shown in Fig.

19

10. They demonstrate once and for all, with their rapid rise with increasing energy, that these fragments originate from compound nucleus decay and compete, in their emission, with the major decay channel, namely neutron emission.
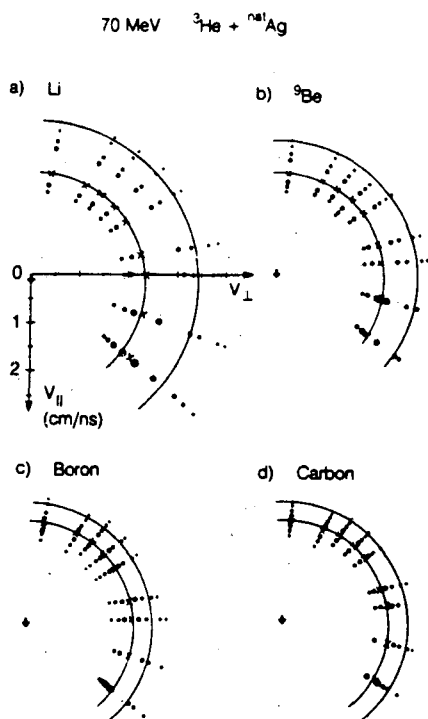

Fig. 8 Invariant cross section plots for representative ejectiles (Li, ^{9}Be, B, and C) for the reaction indicated above. The diameter of the dots is proportional to the logarithm of the cross section and the x's indicate the peak of the velocity distributions. The large arcs are sections of circles centered on the c.m. velocity (center arrow) appropriate for complete fusion. The beam direction (0°) is indicated by the c.m. velocity vector (Sobotka, 1983).
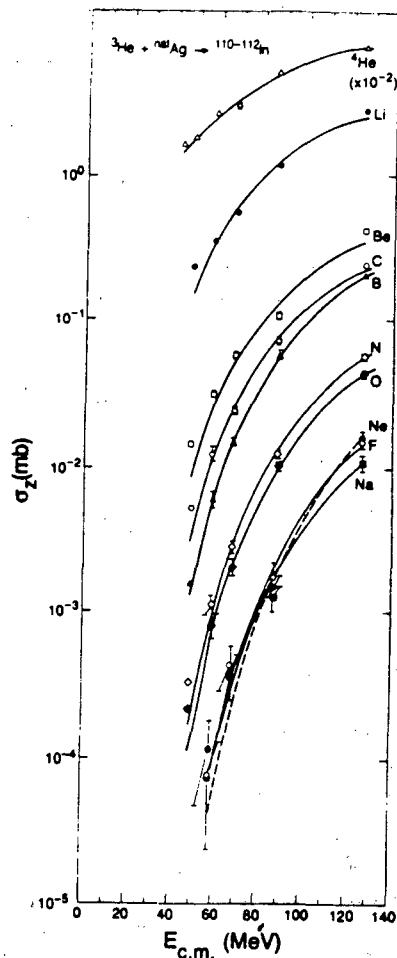
Fig. 9 Dependence of the total integrated cross sections (symbols) for emission of complex fragments on the center-of-mass energy, $E_{c.m.}$, in the reaction ^{3}He + ^{nat}Ag. The curves are compound nucleus fits to the data (McMahan, 1985).

The compound nucleus fits shown in the same figure, on the one hand demonstrate quantitatively the agreement with the compound nucleus hypothesis, and on the other allow one to extract the conditional barriers. The extracted barriers are presented in Fig. 11 together with two calculations (Sierk, 1986). The standard liquid-drop model fails dramatically in
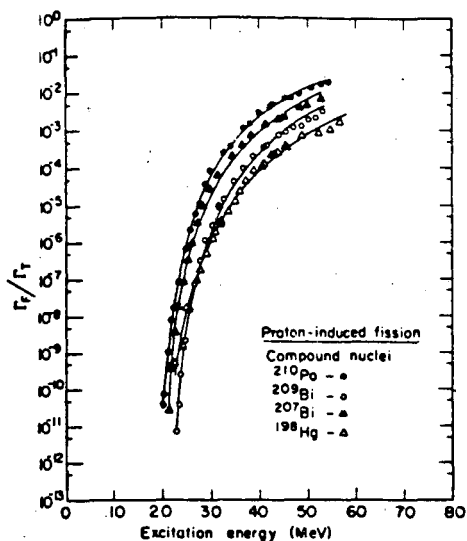
Fig. 10 Fission probabilities of some compound nuclei produced with proton bombardment (Moretto, 1972a).
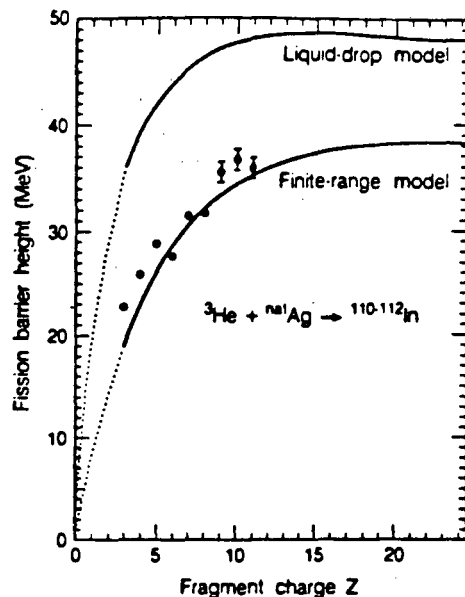
Fig. 11 Calculated (Sierk, 1986) and experimental (McMahan, 1985) conditional fission barriers as a function of the lighter fragment charge for the fission of ^{111}In. The experimental values are obtained from the fits in Fig. 9. The calculated curves for the liquid drop and finite-range models are shown. The dotted portions of the curves are extrapolations.

reproducing the barriers, while the finite-range model, accounting for the surface-surface interaction (so important for these highly indented conditional saddle shapes) reproduces the experimental values almost exactly. This is a most important result, since it determines with great precision crucial points in the potential energy surface and lends confidence to a model that can be used to calculate the same potential energy landscape. The oscillations seen in the data are bigger than the experimental errors and are believed to be due to shell effects associated with the conditional saddle shapes.

Additional studies at low energies demonstrated the role of the potential energy along the ridge line (Sobotka, 1984). As was shown previously, the charge distribution is U shaped or has an additional maximum at symmetry depending on whether the system is below or above the Businaro-Gallone point. The three reactions ^{74}Ge + ^{9}Be, ^{93}Nb + ^{9}Be and ^{139}La + ^{9}Be studied at 8.5 MeV/u produce compound nuclei well below, near, and well above the Businaro-Gallone point, respectively. The observed fragments are emitted from a source with compound nucleus velocity and are characterized by center-of-mass Coulomb-like energies. Their charge distributions are shown in Fig. 12 together with the corresponding compound nucleus calculations. As expected, the U-shaped distributions prevailing at or below the Businaro-Gallone point as exemplified by the ^{76}Ge + ^{9}Be and ^{93}Nb + ^{9}Be

21

reactions, develop in the case of ^{139}La + ^{9}Be a central peak, characteristic of systems above the Businaro-Gallone point. The solid curves in the same figure represent calculations based on the compound nucleus hypothesis.

A final illustration of low energy compound nucleus emission of complex fragments in very heavy systems is given in Fig. 13, where the measured charge distribution (Sarantites, 1988) is given for the reaction ^{232}Th + ^{12}C → [^{244}Cm*] → Z + (96 – Z). The light fragments appearing with yields a factor of 10^5 below the maximum of the distribution were first detected radiochemically and were assumed to be associated with ternary fission (MacMurdo, 1969). However, in this experiment they are proven to be binary events like the rest of the fission fragments.   In fact, the ratio of their yield to the yield at the maximum of the curve is well accounted for by the ratio

$$R = T^*_{BG} \, \rho^*(E - B_{BG})/T_{SS} \, \rho^* (E - B_{SS}) \qquad (49)$$
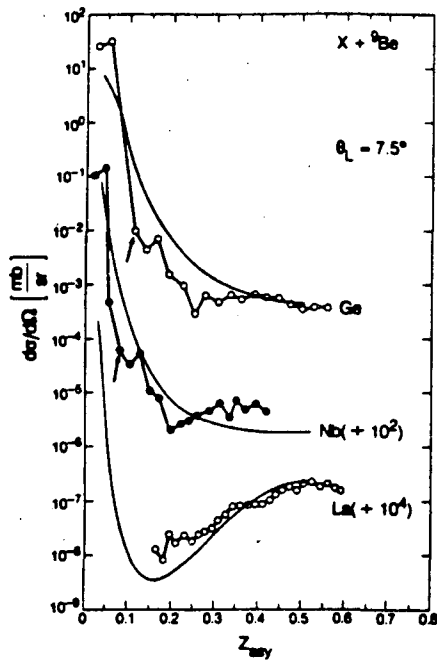
Fig. 12 Center-of mass cross sections (Sobotka, 1984) for products from the 8.5 MeV/u ^{74}Ge, ^{93}Nb, ^{139}La + ^{9}Be systems detected at θ_{lab} = 7.5°. The solid line is a compound nucleus calculation of the fragment yield at $\theta_{c.m.}$ = 30°. The arrows indicate the entrance-channel asymmetry. Data below Z_{asy} = 0.15 were not obtained for the ^{139}La + ^{9}Be system, because of the limited dynamic range of the telescope.
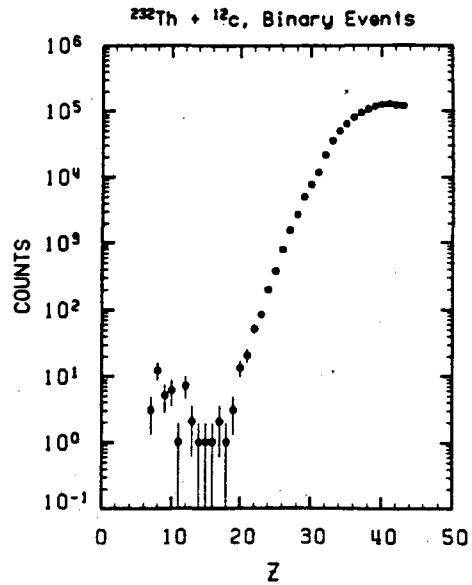
Fig. 13 Experimental charge distribution for binary events from the 8.4 MeV/u ^{232}Th + ^{12}C reaction. The very light fragments arise also from binary decay rather than from ternary fission as previously believed (Sarantites, 1988).

22

where ρ^* are the level densities, T_{BG} and T_{SS} are the temperatures at the Businaro-Gallone mountain of height B_{BG} and at the symmetric saddle of height B_{SS}. Agreement is obtained only if B_{SS} and B_{BG} are calculated with the finite-range model (Sierk, 1986).

3.2 Effects of the angular momentum on complex fragment emission

The role of angular momentum in complex fragment emission has been already illustrated in the dependence of the ridge line upon angular momentum as shown in Fig. 2. The predicted effect of angular momentum has been demonstrated (Sobotka, 1987) by comparing the charge distributions from the reaction ^{93}Nb + ^{9}Be at 8.5 MeV/u with that from the reaction ^{45}Sc + ^{65}Cu at 4.44 MeV/u. These two reactions produce similar compound nuclei with similar (low) excitation energies (78 and 94 MeV, respectively) but with very dissimilar angular momenta (34ħ and 70ħ, respectively) for the highest ℓ wave leading to fission).

The two charge distributions are shown in Fig. 14. Despite the similarity in the excitation energies, the cross sections are very different, the latter cross sections exceeding the fomer by as much as a factor of several hundreds. This impressive increase in cross section is due to the larger angular momentum which substantially decreases the emission barriers. A quantitative confirmation of the effects is shown by the calculations, which use the angular momentum dependent conditional barriers calculated by Sierk. The charge distributions are nicely reproduced for both reactions, although the overprediction in the low Z region for the ^{45}Sc + ^{65}Cu reaction suggests that the calculated barriers in this region are somewhat too low. The evolution in shape brought about by the angular momentum increase is particu-

Fig. 14 Differential cross sections for the 4.44 MeV/u ^{45}Sc + ^{65}Cu (solid symbols) and 8.5 MeV/u ^{93}Nb + ^{9}Be (open symbols) systems. The solid lines are the compound nucleus calculations(Sobotka, 1987).

larly impressive as it shows the strong development of a symmetric peak expected from the shape of the ridge lines at high angular momenta.

The understanding of the role of angular momentum in the ^{45}Sc + ^{65}Cu reaction is demonstrated further in Fig. 15. In this figure the first and second moments of the associated gamma ray multiplicites are plotted vs. Z value. The rise of the average multiplicities at low Z values is understood as a consequence of the partition of the angular momentum among the nascent
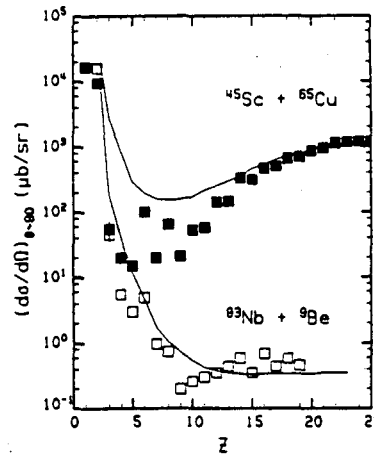
23

fragments for a rigidly rotating configuration at the ridge line. The calculations seem to reproduce the experimental data quite well.
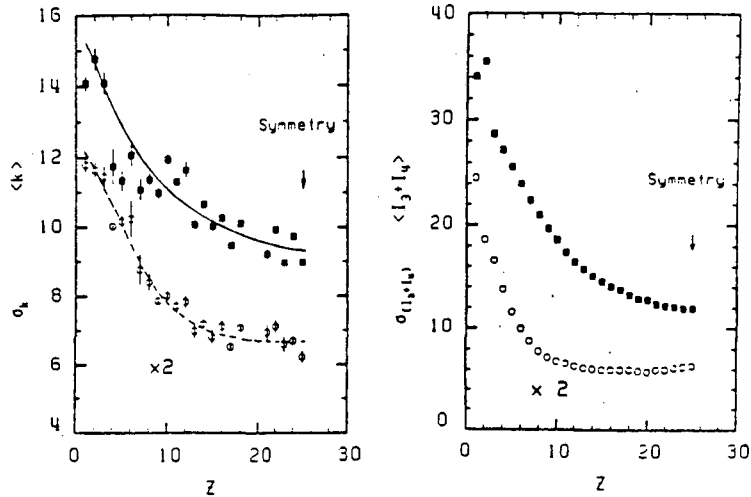

Fig. 15 a) First two moments of the experimental gamma ray multiplicity distributions. b) First two moments of the calculated transferred spin distributions. An approximate comparison with the data in a) can be obtained by dividing the calculated quantities by two.

3.3 Compound nucleus emission at higher energies

Compound nucleus emission of complex fragments at low energy implies an even more abundant emission at higher energies, provided that compound nuclei are indeed formed.

Part of the initial confusion about complex fragment emission at intermediate energies may have been due to the broad range of compound and non compound nucleus sources associated with the onset and establishment of incomplete fusion. This problem can be minimized to some extent by the choice of rather asymmetric systems. In such systems, the range of impact parameters is geometrically limited by the nuclear sizes of the reaction partners. Furthermore, the projectile-like spectator, if any, is confined to very small masses, and does not obscure other sources of complex fragments.

Before proceeding to present some data, it may be useful to anticipate some of the conclusions. The general picture that has emerged is rather simple, at least for relatively asymmeric systems. At sufficiently low energies complete fusion is achieved for most ℓ waves. A compound nucleus is formed which decays and produces, at times, complex fragments. Higher ℓ waves do not lead to fusion, but to quasi elastic and deep inelastic reactions. All decays, both compound and non compound, are essentially binary.

As the bombarding energy increases, the ability of the nuclei to stand each other's impact diminishes so that, starting from the larger impact

parameters and progressively moving into the smaller ones, incomplete fusion sets in. Typically, it is the smaller partner that bears the brunt of the impact, so that only the part of the light nucleus occluded by the larger nucleus fuses with the latter. The result is a light spectator and a fused product which relaxes into a compound nucleus and decays as such. We choose to call this incomplete fusion product "compound nucleus", considering the statistical decay as the essence of a compound nucleus and the complete fusion only a peripheral aspect. In what follows we shall speak of the "binary decay" of this "compound nucleus" despite the fact that a third body, the spectator from the light reaction partner is also present. Above the incomplete fusion "threshold", one can observe a variety of reactions: 1) quasi and deep inelastic; 2) incomplete fusion with light spectator and evaporation residue; 3) incomplete fusion with light spectator and two complex fragments arising from the binary decay of the compound nucleus.

Incomplete fusion or massive transfer appears to begin at approximately 18 MeV/u bombarding energy and extends probably higher than 100 MeV/u. At even higher bombarding energies, it may be replaced by a participant-spectator mechanism in which the interacting nucleons form a fireball physically separated from the rather cool spectators.

In order to illustrate this picture, we are going to follow the compound nuclear emission of complex fragments, as well as other processes, from the lowest energies up to 100 MeV/u. The reactions studied were: ^{93}Nb, ^{139}La + ^{9}Be,^{12}C,^{27}Al from 8.5 MeV/u up to 50 MeV/u (Auger, 1985, 1987; Bowman,1987; Charity, 1986, 1988, 1988a, 1988b); ^{139}La + ^{12}C,^{27}Al from 14 to 100 MeV/u (Charity, 1988b; Bowman, 1988); as well as the lighter systems ^{63}Cu + ^{12}C,^{27}Al at 12.6 MeV/u (Han, 1988).

These reactions were studied in reverse kinematics in order to facilitate the detection of all of the fragments over most of the center-of-mass angular range. The use of reverse kinematics is particularly useful because it carries a most powerful signature for binary decays producing fragments with Coulomb-like energies. Figure 16 gives an example of such a signature, as it appears on line from the output of a ΔE-E telescope. For each atomic number, characterized by its own hyperbola, two energy components are clearly visible.

The explanation of these components is given in Fig. 17. In this figure we show a schematic diagram of the invariant cross section in the $v_{\parallel}$ - $v_{\perp}$ plane for the compound binary emission of a given fragment. The circle represents the expected Coulomb ring associated with binary
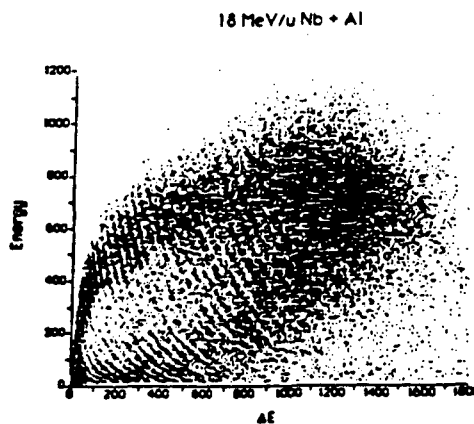
18 MeV/u Nb + Al

Fig. 16 Density plot of ΔE-E for the reaction 18 MeV/u ^{93}Nb + ^{27}Al for fragments detected from 4° to 10°. Notice the two kinetic energy components associated with each element characterized by a hyperbolic ridge in the distribution (Charity, 1988a).

25

isotropic compound emission in the center of mass. The radius of the circle decreases monotonically with increasing fragment charge. A given angle, in the lab system, intersects each circle in two points. In other words, a given lab angle corresponds to two c.m. angles, one forward, and the other backward. This explains the two components observed in Fig. 16. As the radius of the Coulomb circle decreases, the two solutions progressively come closer together, until they coincide and eventually disappear altogether. This is seen in Fig. 16 and in its translation into an invariant cross section plot in the Z - v plane shown in Fig. 18. In the latter figure the two legs of the lambda (Λ) pattern correspond to the two solutions. The tip of the Λ is the last Z value detectable at the chosen lab angle.

As can be readily seen, the presence of the two components in the E-ΔE plane suggests immediately a variety of conclusions: 1) The fragments are emitted from a source with a well defined velocity; 2) The fragments are emitted in a binary decay; 3) the fragment's Coulomb energy indicates a
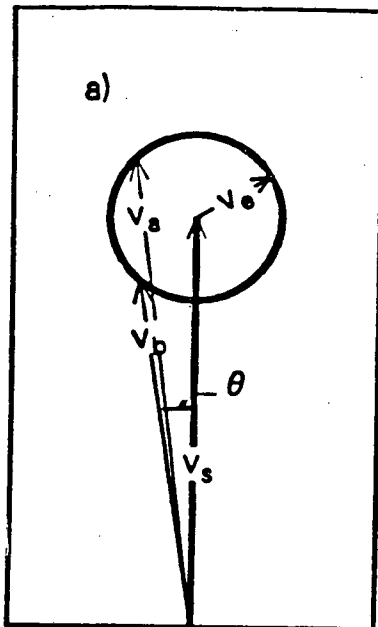
Fig. 17 Schematic representation of reverse kinematics for the emission of a complex fragment in a compound-nucleus binary decay. V_s is the lab. source velocity, V_e is the Coulomb-like velocity of the fragment in the source frame, while V_a and V_b are the two velocity components at the lab angle θ.

18 MeV/u Nb + Be
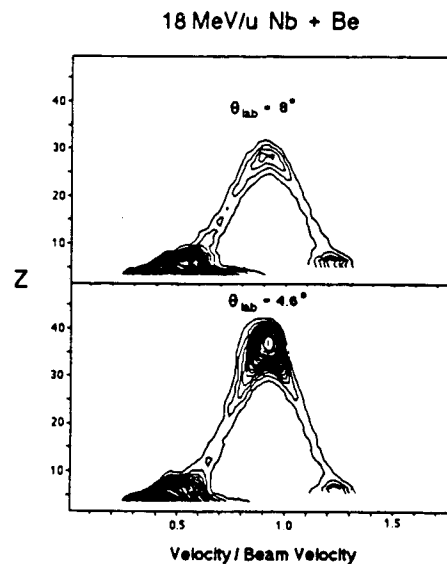
Fig. 18 Contours of the invariant cross section in the Z - velocity plane for complex fragments emitted from the 18 MeV/u [93]Nb + [9]Be reaction at θ_{lab} = 4.6° and 8°. The "big foot" visible at low velocities for Z < 10 is attributed to quasi elastic and deep inelastic products (Charity, 1988a).

26

complete thermal relaxation characteristic of a compound nucleus decay or completely damped deep inelastic reaction. In this sense we believe that plots like those of Fig. 16 & 18 represent a powerful signature for compound nucleus emission.

As we mentioned above, reverse kinematics allows one to cover a large c.m. angular range with only a moderate coverage of lab angles. Consequently, it is possible to reconstruct invariant cross sections in the $v_{\parallel}$ - $v_{\perp}$ plane for each atomic number rather readily. A few examples are shown in Figs. 19, 20 & 21. For all the reactions studied so far one has observed beautifully developed Coulomb rings whose isotropy indicate that, up to the highest bombarding energies, the fragments do in fact arise from binary compound nucleus decay. Only the fragments in the neighborhood of the target atomic number show the presence of an additional component at backward angles (big foot), that can be attributed to quasi elastic and deep inelastic processes, and/or to the spectator target-like fragment in the incomplete fusion reactions prevailing at higher bombarding energies.
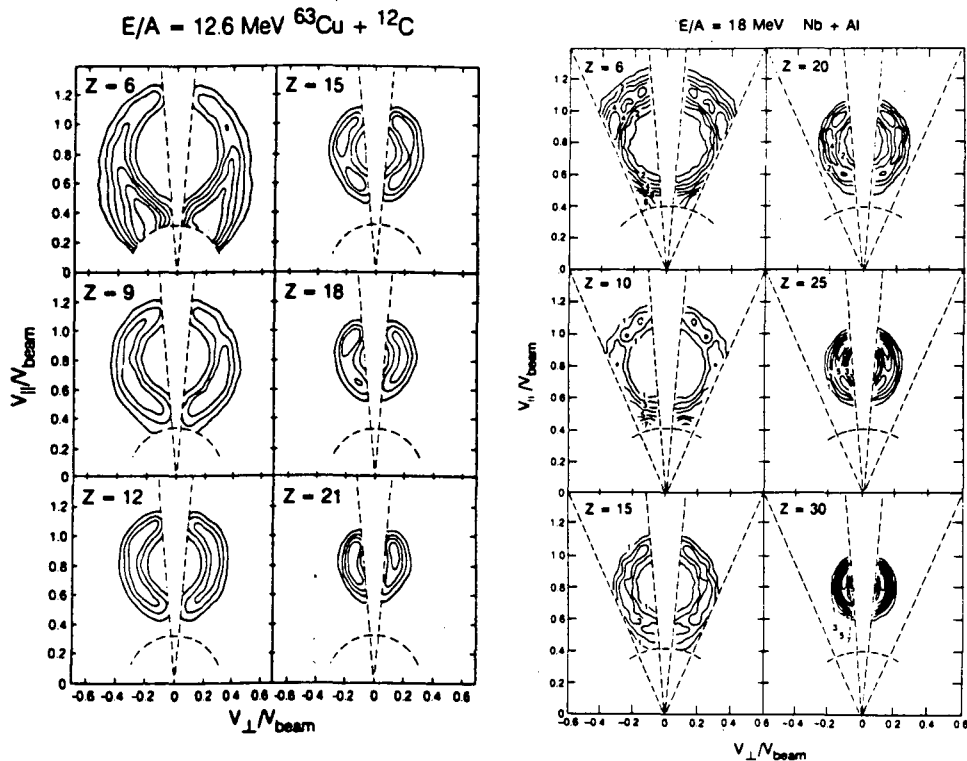
Fig. 19 Contours of the experimental cross section $\partial^2\sigma/\partial V_{\parallel}\partial V_{\perp}$ in the $V_{\parallel}$-$V_{\perp}$ plane for representative fragments detected in the reactions: a) E/A = 12.6 MeV ^{63}Cu + ^{12}C and b) E/A = 18 MeV ^{93}Nb + ^{27}Al. The beam direction is vertical towards the top of the figure. The dashed lines show the maximum and minimum angular thresholds and the low velocity threshold of the detectors. The magnitudes of the contour levels indicated are relative (Han, 1988; Charity, 1988a,b).
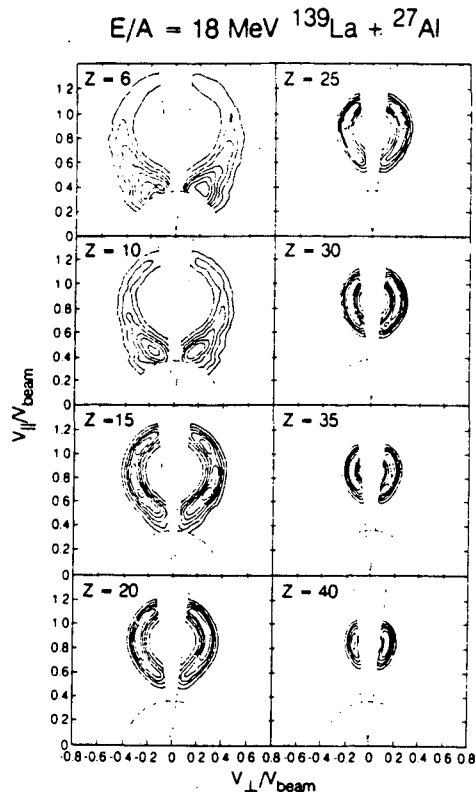
E/A = 18 MeV ^{139}La + ^{27}Al

30 MeV/u Nb + Be

11 ≤ Z ≤ 17

Fig. 19c Contours of the experimental cross section $\partial^2\sigma/\partial V_{||}\partial V_\perp$ in the $V_{||}$-$V_\perp$ plane for representative fragments detected in the reactions E/A = 18 MeV ^{139}La + ^{12}C. See Fig. 19.
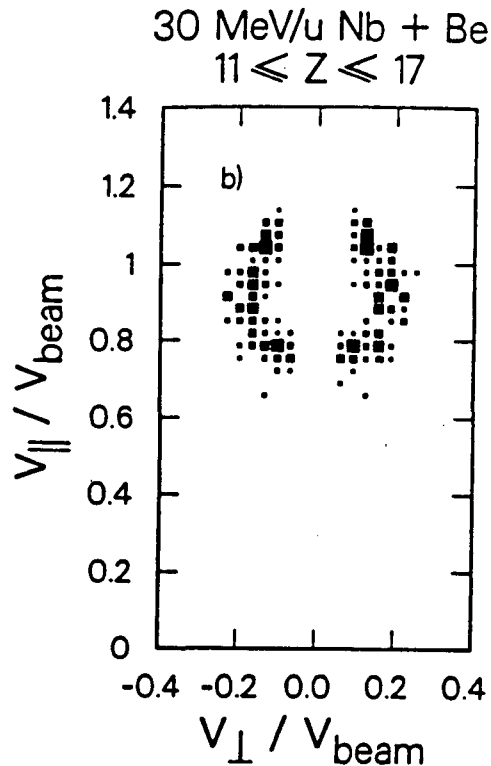
Fig. 20 Density plot of the cross section in the $V_{||}$ - $V_\perp$ plane for fragments of 11 ≤ Z ≤ 17 for the reaction 30.3 MeV/u ^{93}Nb + ^{9}Be (Charity, 1988).

The centers of these rings provide us with the source velocities for each Z value. For a variety of reactions, these source velocities are shown in Figs. 22 - 24 as a function of the fragments' atomic number. For all bombarding energies the source velocity is independent of the fragments' Z value. Up to ~18 MeV/A, one can conclude that a single source with compound nucleus velocity is responsible for the emission of all the fragments. As the bombarding energy increases, it appears that incomplete fusion sets in. The observed source velocities are intermediate between the projectile and compound nucleus velocities. In the case of 50 MeV/A ^{139}La + ^{12}C, the source velocity is halfway between the two limits, indicating that ~1/2 of the ^{12}C target fuses with the ^{139}La projectile. It is truly remarkable that ven when incomplete fusion sets in, the source velocity is independent of Z value and quite sharp.

The radii of the Coulomb rings give the emission velocities in the center of mass. These mean velocities with their standard deviations are shown as a function of Z value in Figs. 22-24 for a variety of reactions. The almost linear

dependence of these velocities upon fragment Z value is a clear indication of their Coulomb origin. This is also supported by their independence of bombarding energy (Charity, 1988a). The Coulomb calculations (lines), which well reproduce the data, further illustrate the degree of relaxation of the c.m. kinetic energy. The variances of the velocities arise from a variety of causes, among which the inherent Coulomb energy fluctuation due to the shape fluctuations of the "scission point", and the fragment recoil due to sequential evaporation of light particles.
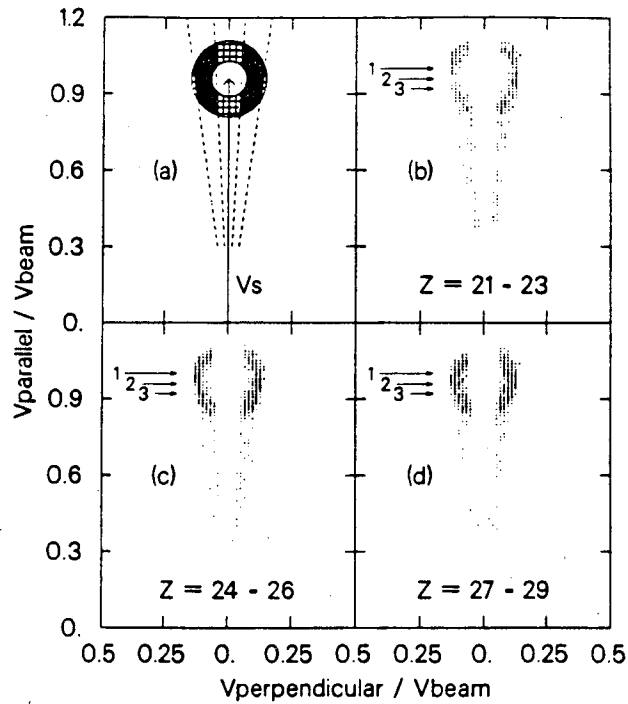
Fig. 21 (a) Schematic representation of complex fragment emission in the $v_{\parallel}$ - $v_{\perp}$ plane from a compound nucleus with velocity v_s. The Coulomb ring is smeared out by sequential evaporation. The geometric limits of the detector are shown by the dashed lines. (b,c,d) Density maps of the inclusive cross section for three Z bins for the reaction ^{139}La + ^{12}C at 50 MeV/u. Arrows 1,2, and 3 denote the beam velocity, extracted source velocity, and the velocity for complete fusion, respectively (Bowman, 1987).

E/A = 12.6 MeV ^{63}Cu + ^{12}C   E/A = 12.6 MeV ^{63}Cu + ^{27}Al
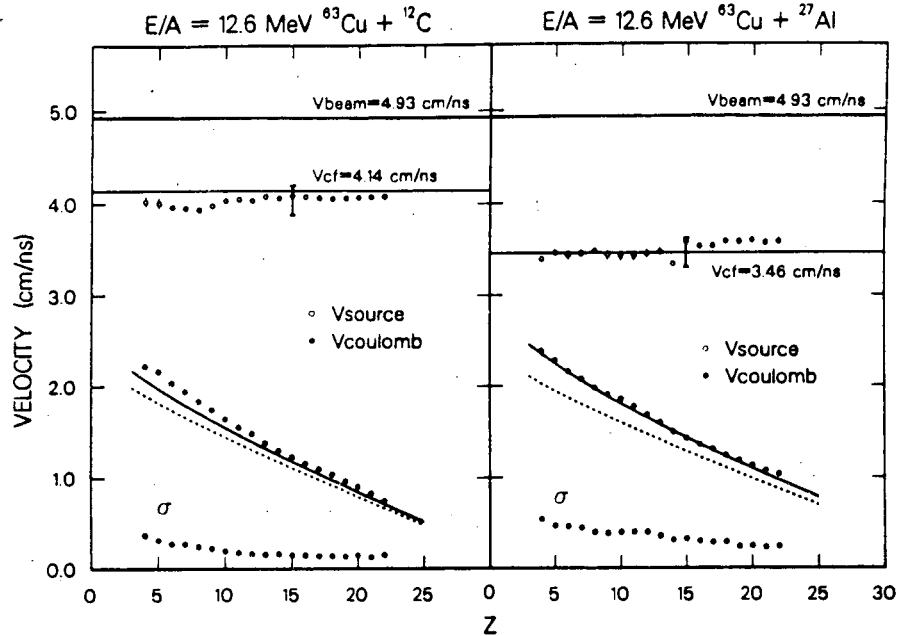
Fig. 22 Source velocities (open symbols) extracted from the Coulomb ring of each Z-species produced in the 12.6 MeV/u ^{63}Cu + ^{12}C,^{27}Al reactions. The small error on each point represents the statistical error associated with the extraction process. The large squared error bars indicate the possible systematic error. The velocities of the beam and the compound system are shown for reference. First and second moments (solid symbols) of the fragments' c.m. velocity spectra for each Z-species (Han, 1988). The dashed lines are Coulomb calculations, while the solid lines include angular momentum effects.

E/A=18 MeV/u La+C   E/A=18 MeV/u La+Al
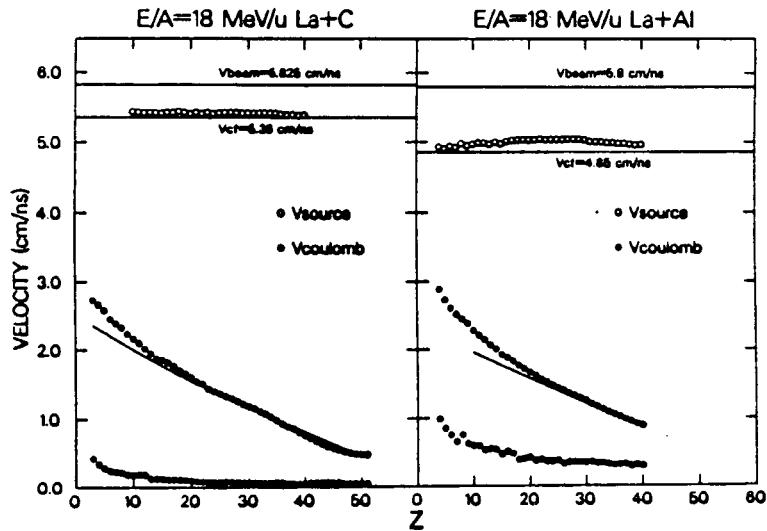
Fig. 23 Source velocities extracted from the Coulomb ring of each Z-species produced in the 18 MeV/u ^{139}La + ^{12}C, ^{27}Al reaction (Charity, 1988b). See Fig. 22.

30
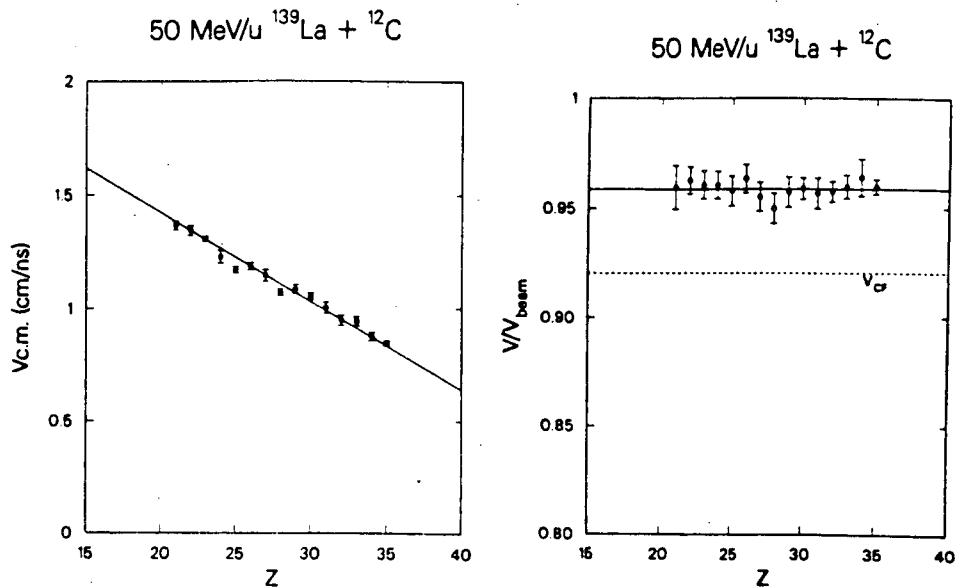
Fig. 24 a) Source velocities extracted from the inclusive data as a function of the fragment Z-value for the 50 MeV/u ^{139}La + ^{12}C reaction. The dotted line represents the velocity for complete fusion and the solid line is the average of the experimental source velocities (Bowman, 1987). b) Extracted c.m. emission velocities, corrected for sequential evaporation. The solid line is a Coulomb calculation, which uses the Viola (1985) kinetic energy systematics.

3.4 Angular distributions

The most important feature of the angular distributions providing diagnostic information regarding compound nucleus emission is their symmetry about 90° in the center of mass. Because of the rather large angular momenta involved in these reactions, one also expects the angular distributions to be of the form $d\sigma/d\Omega = 1/\sin\theta$ or $d\sigma/d\theta = $ constant. This would also correspond to an isotropic distribution along the Coulomb rings, well documented in Figs. 19, 20 and 21. In contrast, the angular distributions of projectile-like fragments and target-like fragments produced in quasi or deep inelastic processes should show a backward and a forward peaking, respectively.

The available data are sufficiently complete to provide information on the angular distribution of individual fragments. These angular distributions are shown in Figs. 25 & 26. In general, one observes angular distributions with a $1/\sin\theta$ dependence ($d\sigma/d\theta = $ constant), except in the vicinity of the target or projectile Z value where quasi elastic, deep inelastic and target spectator fragments manifest themselves with a forward or backward peaking.

For the ^{12}C target, the backward peaking of the target-like fragment is quite visible in all the cases. It is most prominent for Z = 4,5 and vanishes for Z ≥ 10. In the case of ^{27}Al target, the backward peak extends up to Z ≅ 13 due to
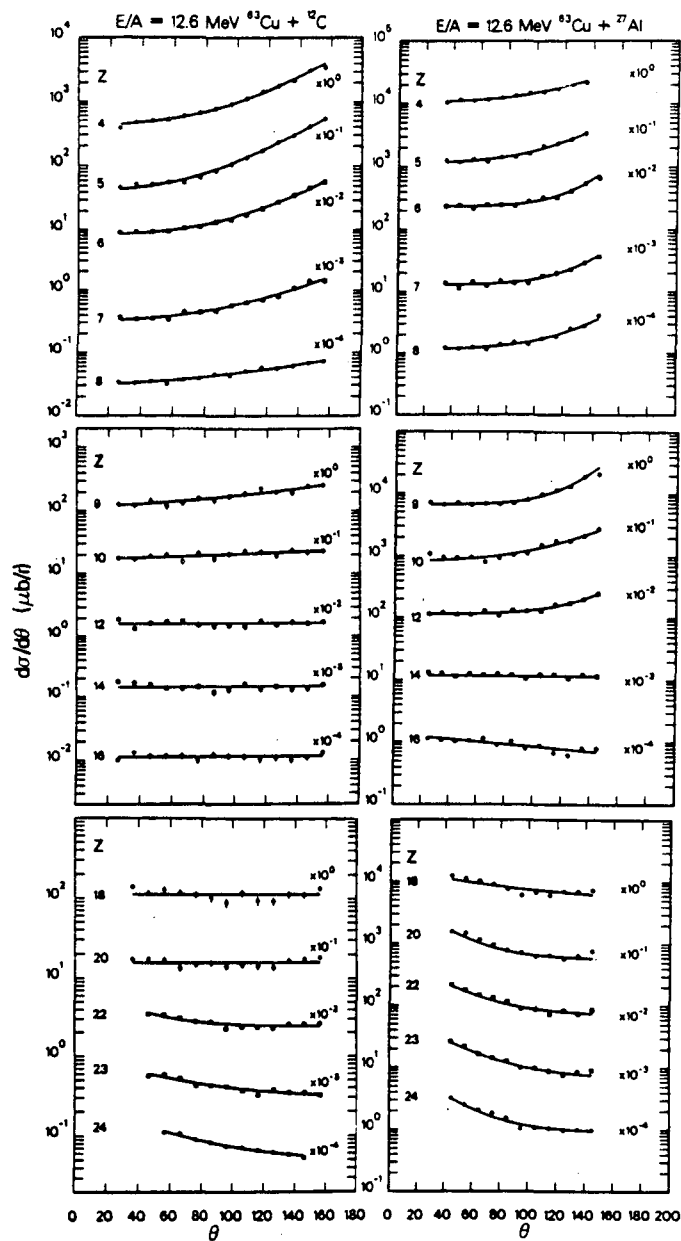
Fig. 25 Angular distributions (dσ/dθ) in the source frame for representative Z values from the 12.6 MeV/u ^{63}Cu + ^{12}C, ^{27}Al reactions. The backward rise at low Z values and the forward rise at high Z values is attributed to target-like and projectile-like (quasi and deep inelastic) products. The angular distributions are flat for products a few Z values larger than the target (Han, 1988).
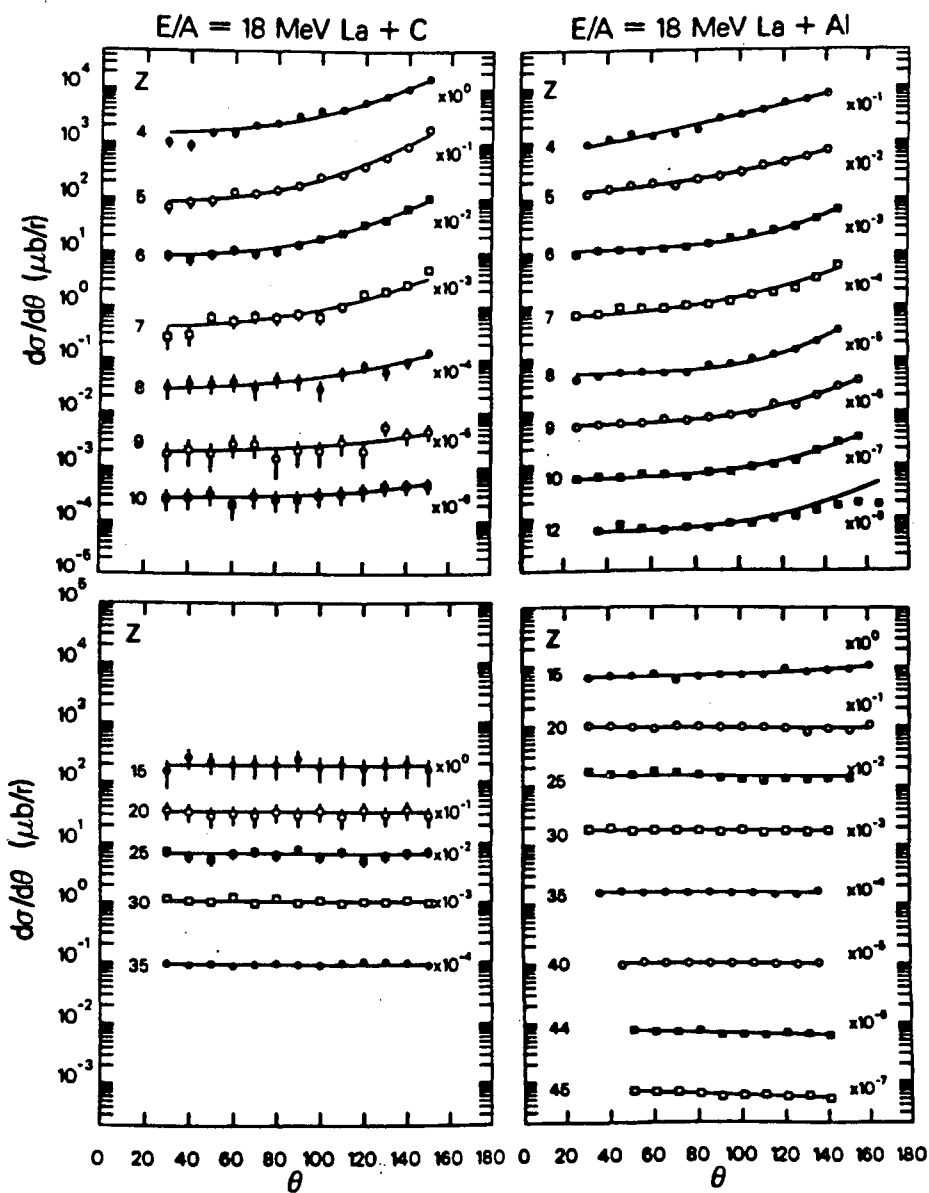
Fig. 26 Angular distributions (dσ/dθ) in the source frame for representative Z values from the 18 MeV/u ^{139}La + ^{12}C, ^{27}Al reaction. The backward rise at low Z values and the forward rise at high Z values is attributed to target-like and projectile-like quasi and deep inelastic products. Note that the cross sections are flat for a large range of Z values intermediate between the target and the projectile (Charity, 1988b).

the larger atomic number of the target. Thus the use of a higher Z target tends to mask the compound nucleus component with quasi and deep inelastic products for a larger number of products. In the same figures, one also observes the forward peaking associated with the projectile-like fragments. The dominance of the quasi and deep inelastic components at atomic numbers near that of the projectile is especially visible in Fig. 25 for the reaction $^{63}Cu + {}^{12}C, {}^{27}Al$ at 12.7 MeV/u.

3.5 Cross sections

All of the evidence presented so far for the intermediate energy complex fragment emission points rather convincingly towards a compound nucleus process. However, the most compelling evidence for this compound mechanism lies in the statistical competition between complex fragment emission and the major decay channels, like n, p, and ^4He emission. The simplest and most direct quantity testing this hypothesis is the absolute cross section.
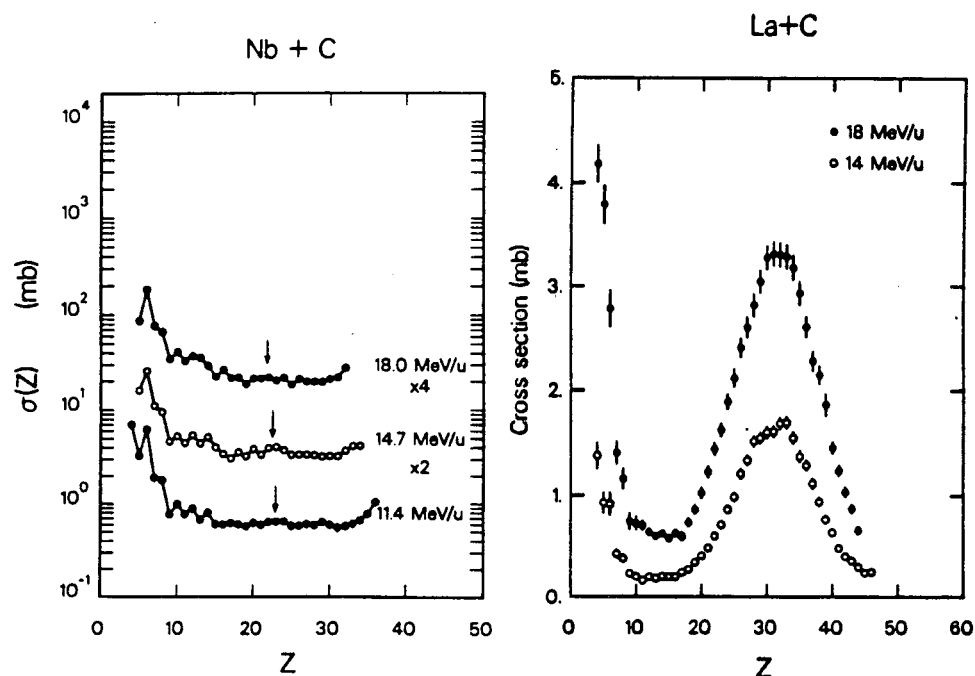

Fig. 27 Angle-integrated charge distributions of complex fragments associated with fusion-like reactions of ^{93}Nb and ^{12}C at three bombarding energies. The arrows indicate the secondary Z-values at each bombarding energy associated with a primary symmetric division (Charity, 1988a).

Fig. 28 Angle-integrated cross sections plotted as a function of the fragment Z-value for the 14 &18 MeV/u $^{139}La + {}^{12}C$ reactions (Charity, 1988b).

Absolute cross sections as a function of Z value are shown in Figs. 27-33. At first glance one can observe a qualitative difference between the charge distributions from the Nb-induced and the La-induced reactions. The former distributions portray a broad minimum at symmetry whereas the latter show a broad central fission-like peak that is absent in the former distributions. This difference can be traced to the fact that the former systems are below or near the Businaro-Gallone point while the latter systems are well above.

In general, for a given system, the cross sections associated with the charge distributions increase in magnitude rapidly at low energies, and very slowly at high energy, in a manner consistent with Eq. 13. However, the shape of the distributions is rather insensitive to the bombarding energy over the energy range explored, although one observes a flattening of the distributions with increasing bombarding energy as predicted also by Eq. 13.

As was said above, the most important information associated with these cross sections is their absolute value and their energy dependence. Through them, the competition of complex fragment emission with the major decay channels, like n, p, and α decay is manifested. This is why we attribute a great deal of significance to the ability to fit such data. Examples of these fits are shown in Figs. 29-32.

Fig. 29 Comparison of experimental and calculated charge distributions for the ^{93}Nb + ^{9}Be reaction at 8.5 MeV/u. The experimental data are indicated by the hollow circles and the values calculated with the code GEMINI are shown by the error bars. The dashed curve indicates the cross sections associated with classical evaporation residues which decay only by the emission of light particles $(Z \leq 2)$ (Charity, 1988a). Note the value of the excitation energy (E^*) corresponding to complete fusion and the value of J_{max} assumed to fit the data.

The calculations are performed with an evaporation code GEMINI (Charity, 1988a) extended to incorporate complex fragment emission. Angular momentum dependent finite-range barriers are used (Sierk, 1986). All the fragments produced are allowed to decay in turn both by light particle emission or by complex fragment emission. In this way higher chance emission, as well as sequential binary emission, are accounted for.
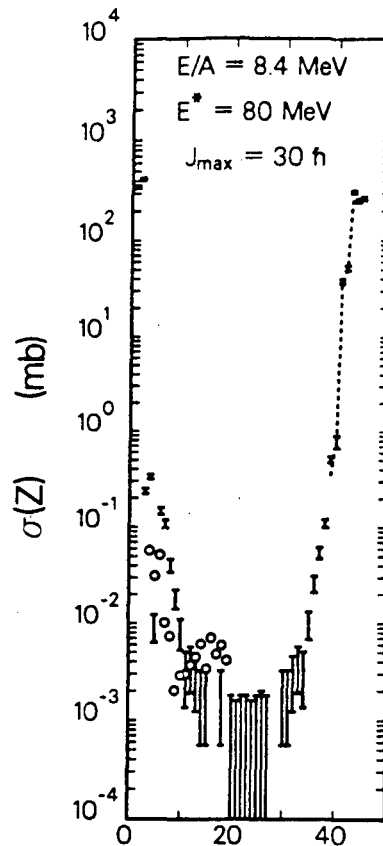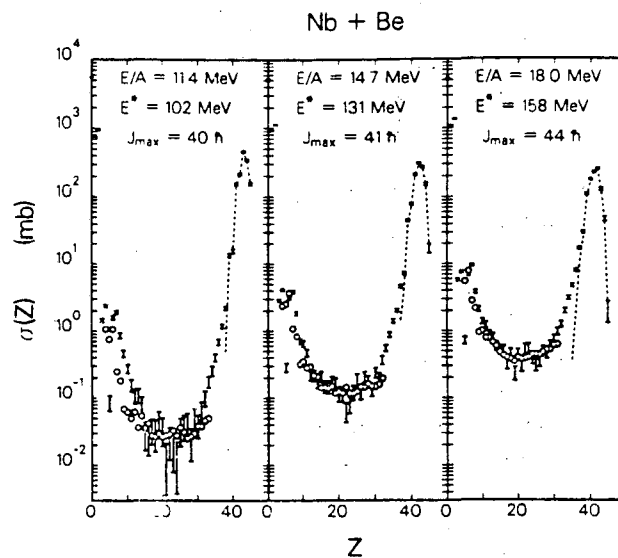
Nb + Be

Fig. 30 Comparison of experimental and calculated charge distributions for the ^{93}Nb + ^{9}Be reaction at E/A = 11.4, 14.7, and 18.0. See Fig. 29.
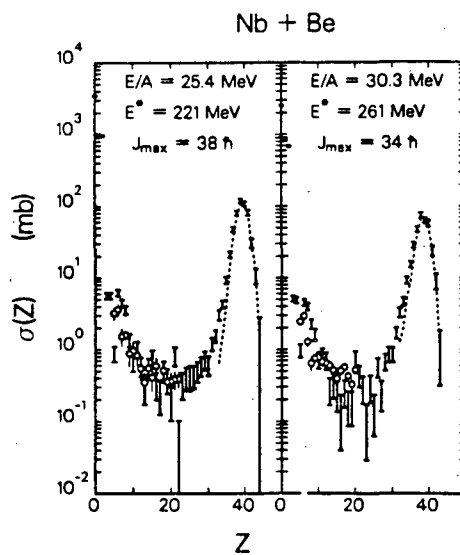
Nb + Be

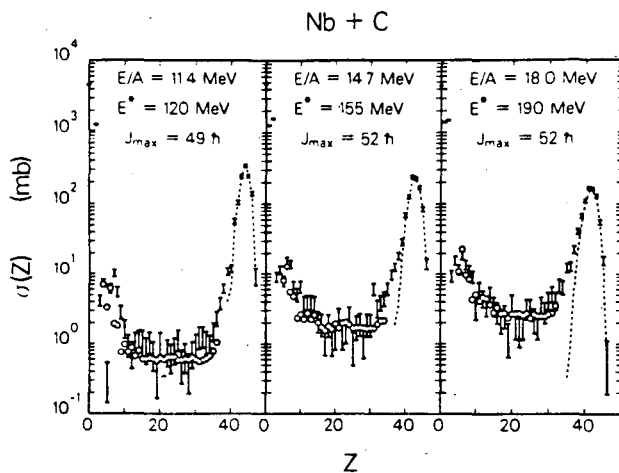Fig. 31 Same as in Fig. 30, for the ^{93}Nb + ^{9}Be reaction at E/A =25.4 and 30.3.

36

Nb + C

Fig. 32 Same as in Fig. 30, for the ^{93}Nb + ^{12}C reaction at E/A = 11.4, 14.7, and 18.0.
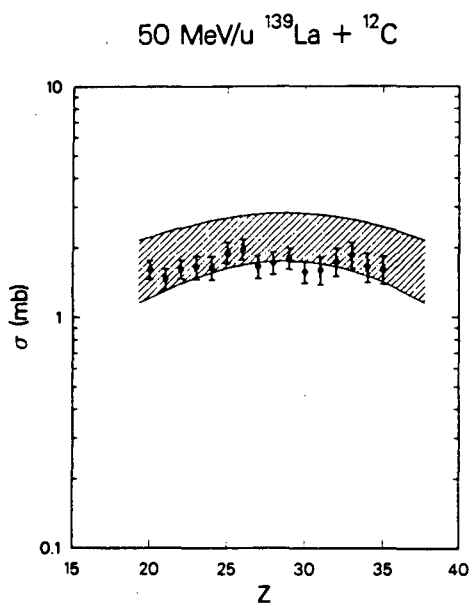
50 MeV/u ^{139}La + ^{12}C

Nb + Be

Fig. 33 Same as in Fig. 30, for the ^{139}La + ^{12}C reaction at E/A = 50. The hatched area indicates the uncertainty of the calculation resulting from uncertainties in excitation energy and angular momentum.
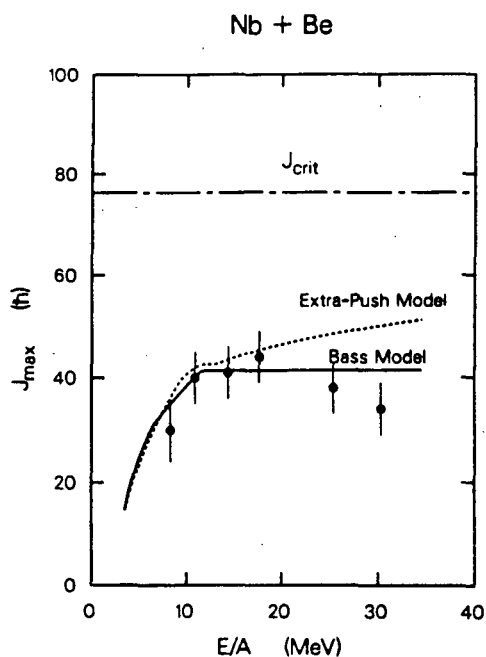
Fig. 34 Plot showing the maximum angular momentum for fusion (J_{max}) obtained by fitting the experimental charge distributions as a function of bombarding energy for the ^{93}Nb + ^{9}Be reactions. The dashed and solid curve show the predictions of the extra-push and Bass models, respectively. The chain dashed lines indicate the angular momentum (J_{crit}) where the barrier for symmetric division vanishes (Charity, 1988a).

37

The cross section is integrated over ℓ waves up to a maximum value that provides the best fit to the experimental charge distributions. In the case of the ^{93}Nb + ^{9}Be & ^{12}C, for bombarding energies up to 18 MeV/A, the quality of the fits is exceptionally good and the fitted values of ℓ_{max} correspond very closely to those predicted by the Bass model (Bass, 1974) or by the extra push model (Swiatecki, 1982), as shown in Fig. 34.

These calculations allow one to evaluate the contribution to the charge distributions of the pure evaporation residues arising solely from the emission of fragments with mass A ≤ 4. This contribution is shown in Figs. 29-32 by the dashed curves. One should note that for these asymmetric reactions below 20 MeV/u, evaporation residues are predicted to be the dominant products of the compound nucleus decay.

At higher bombarding energies, as incomplete fusion sets in, there is a slow decline in the complex fragment production cross section due to the relative decrease of the excitation energy and angular momentum. Fig. 35 shows that the maximum in the cross section is achieved around 18 MeV/A, just before the onset of incomplete fusion. Above this bombarding energy, it is possible to reproduce all the cross sections by means of compound nucleus decay of the incomplete fusion product (Charity, 1988).

This remarkable success in reproducing the absolute charge distributions over a bombarding energy range of 8.5 to 35 MeV/u for the ^{93}Nb + ^{9}Be & ^{12}C reactions demonstrates that the compound nucleus mechanism characterized at the lowest energies dominates the picture at intermediate energies. It seems fair to say that, for atomic numbers between projectile and target, the compound nucleus mechanism accounts for all of the fragment emission, while for the remaining Z range it constitutes an important component, together with the quasi elastic and deep inelastic processes which are abundantly represented in this region. As we have seen, in the range of reactions considered so far, binary decay is dominant. However, it is an easy prediction that, even when we enter the energy range where ternary and higher multiplicity events dominate, the compound nucleus mechanism will account for a great deal if not all of the fragment emission through sequential binary decay.
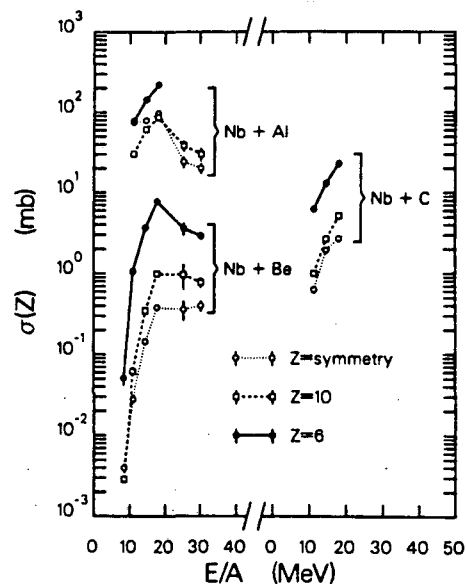

Fig. 35 Excitation function for representative complex fragment species. The Z-value associated with symmetric division was obtained from the coincidence data (Charity, 1988a).

3.6 Coincidence data

If any doubt still remains concerning the binary nature of the decay involved in complex fragment production, it can be removed by the detection of binary coincidences. Several examples of $Z_1 - Z_2$ correlations are shown in Figs. 36 & 37. Some examples of the sum ($Z_1 + Z_2$) spectra are also shown in Figs. 38 & 39. One can observe the binary band in the $Z_1 - Z_2$ correlation as a general feature persisting up to the highest bombarding energies (100 MeV/u for $^{139}La + ^{12}C$)! The binary nature is proven by the correlation angles as well as by the sum of the fragments' atomic numbers which accounts for most of the target + projectile charge. The missing charge can be accounted for by the extent of incomplete fusion and by the sequential evaporation of light charged particles ($A \leq 4$). A particularly interesting example of this verification is shown in Fig. 40 for the reactions $^{93}Nb + ^{12}C, ^{27}Al$. In this figure, the average charge sum $Z_1 + Z_2$ is shown as a function of Z_2. The dashed lines indicate the charge of the compound nucleus obtained in an incomplete fusion process as calculated from the measured source velocities. The solid lines show the reduction in charge brought about by evaporation from the hot primary fragments formed in the binary decay. The excitation energy of the fragments was evaluated on the basis of the source velocity, which tells about the extent of incomplete fusion. The remarkable agreement of these calculations with the data, which is retained over a large range of excitation energies speaks for the internal consistency of such an analysis.

This same consistency holds over a very wide range of bombarding energies (8.5 - 30.3 MeV/u). In Fig. 41 the average sum of the symmetric products' final atomic numbers for the reaction $^{93}Nb + ^{27}Al$ is plotted vs bombarding energy. The five experimental points correspond to bombarding energies of 11.4, 14.7, 18, 25.4 and 30.3 MeV/u. The solid line represents the sum of the target and projectile atomic numbers. The long dashed line corresponds to the compound nucleus atomic number calculated on the basis of the momentum transfer systematics (Viola, 1982) in incomplete fusion. The short dashed line corresponds to the sum of the charges of the final fragments after evaporation as calculated with the code PACE (Gavron, 1980). The agreement between calculation and experiment is very satisfactory and
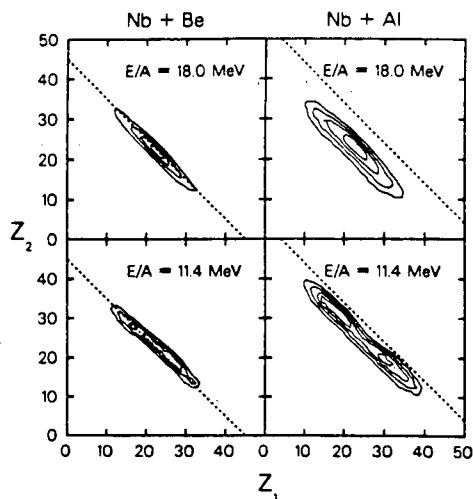

Fig. 36 Representative Z_1-Z_2 contour plots for coincidence events from the reactions $^{93}Nb + ^9Be$ & ^{27}Al at 11.4 and 18.0 MeV/u. Z_1 and Z_2 refer to the Z-values of fragments detected in two detectors at equal angles on opposite sides of the beam (Charity, 1988a)
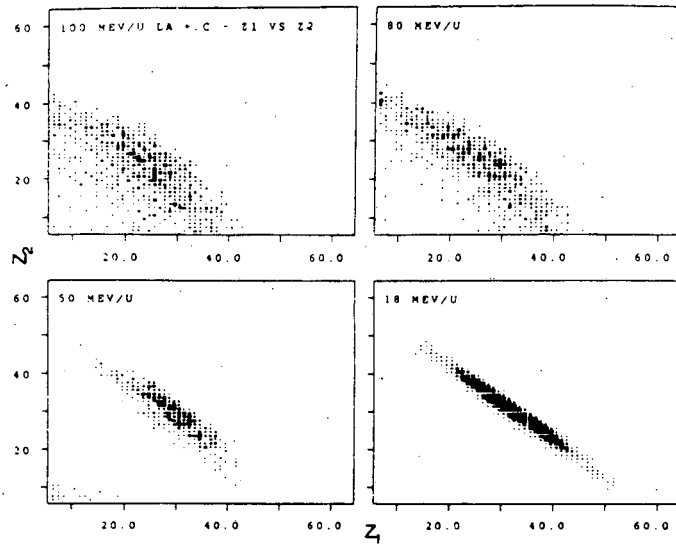
Fig. 37 Scatter plots of the experimental Z_1 - Z_2 correlation for coincident fragments detected at symmetric angles on opposite sides of the beam in the $^{139}La + ^{12}C$ reactions at 18, 50, 80, and 100 MeV/u (Charity, 1988b; Bowman, 1987, 1988).
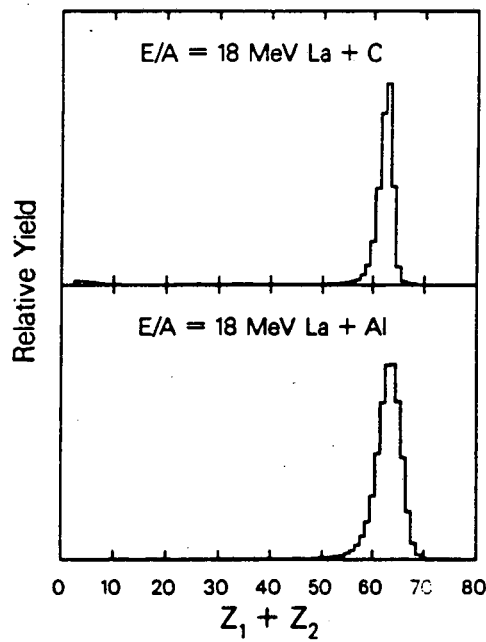

Fig. 38 The relative yield of coincidence events plotted as a function of the sum of the atomic charges of the two coincident fragments for the $^{139}La + ^{12}C$ & ^{27}Al reactions at 18 MeV/u (Charity, 1988b).
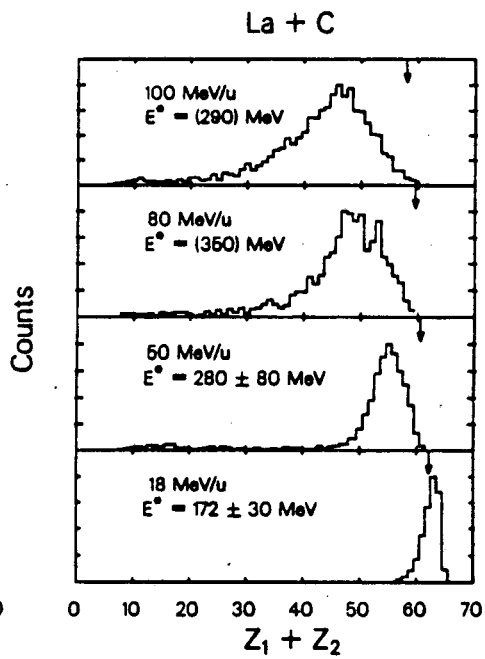
Fig. 39 The relative yield of coincidence events plotted as a function of the sum of the atomic charges of the two coincident fragments for the $^{139}La + ^{12}C$ reactions at 18, 50, 80 and 100 MeV/u.
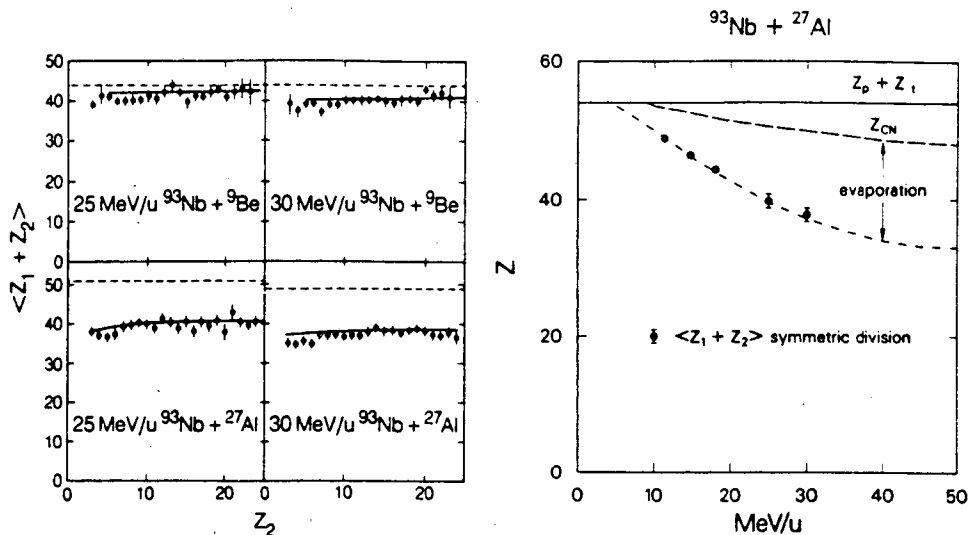
$^{93}Nb + ^{27}Al$

Fig. 40 The mean sum, $<Z_1 + Z_2>$ of coincidence events plotted as a function of Z_2 for the $^{93}Nb + ^9Be$ & ^{27}Al reactions at 25.4 and 30.3 MeV/u. The dashed lines indicate the average charge of the source system estimated from the mass transfer. The charge loss for binary events due to sequential evaporation was estimated using the evaporation code PACE, and the residual $Z_1 + Z_2$ values are indicated by the solid curves (Charity, 1988).

Fig. 41 Comparision of the experimentally determined sum of the charges for symmetric products with calculations performed on the basis of incomplete fusion and sequential evaporation from the primary binary fragments. Data points are shown for five bombarding energies for the $^{93}Nb + ^{27}Al$ reaction.

supports our basic understanding of incomplete fusion, mass and energy transfer, as well as of sequential evaporation.

Finally, it is possible to verify that the coincidence rate and the single rate are consistent with each other under the assumption that all the fragments arise from binary decay. This can be done by evaluating the experimental coincidences/singles ratio on one hand, and on the other by computing the same ratio from the singles rate and from the knowledge of the efficiencies of the detectors involved in the coincidence measurement. In Fig. 42 & 43 the comparison between the experimental and calculated coincidence efficiencies is shown for some reactions. The good agreement which is observed indicates that all of the coincidences can be accounted for by the singles data. In other words, all the singles data are associated with binary processes.
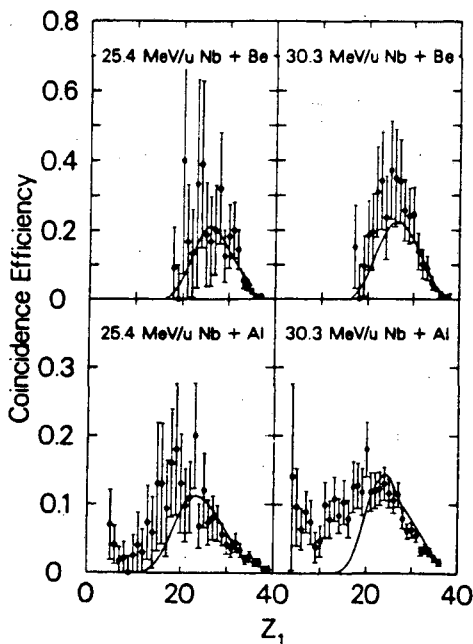
Fig. 42 The coincidence efficiency (ratio of the coincidence yield to the inclusive yield) measured in Detector 2 plotted as a function of the fragment Z-value in Detector 1 for the ^{93}Nb + ^{9}Be & ^{27}Al reactions at 25.4 and 30.3 MeV/u. The solid curves show the results of a Monte Carlo simulation of the binary decay of a hot compound nucleus (Charity, 1988).
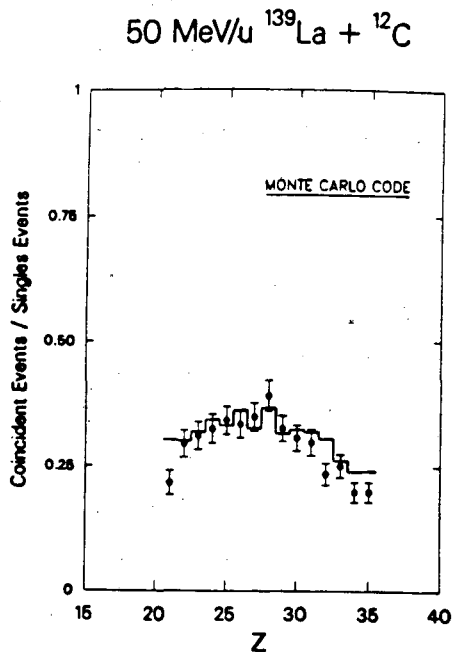
Fig. 43 The experimental coincidence/ singles ratio compared to a Monte Carlo simulation for the ^{139}La + ^{12}C reaction at 50 MeV/u (Bowman, 1987).

4. Outlook and Conclusions

The explicit treatment of the mass asymmetry degree of freedom has allowed us to extend the concept of fission to statistical processes involving the emission of fragments of any size. This generalization makes fission a process that extends throughout the periodic chart and that incorporates as special cases both traditional fission and light particle evaporation. We have developed this generalization in the theoretical section of this paper. In the experimental section, we have tried to document this process in a variety of regimes ranging in mass from relatively light to medium-heavy systems and in energy from near the absolute barrier up to 100 MeV/u bombarding energies.

At this stage it seems safe to conclude that the statistical emission of complex fragments as a generalized fission process is well established and its role has been proven important from the lowest excitation energies up to the limits of compound nucleus stability.

Despite the extensive research covered in this presentation, a lot if not most of the work remains yet to be done. The experimental determination of the conditional barriers is so far limited to one isotope and even that is

incomplete. A systematic study of the conditional barriers is clearly necessary to test the validity (or to define the parameters) of the macroscopic models like the finite range model. As it has been done for the symmetric barriers in heavy systems, it should be possible to isolate the shell effects from the macroscopic part of the conditonal barriers. Furthermore, the knowledge of the conditional barriers is essential for the predictions of cross sections and reaction rates.

A natural development of these studies should lead to the evaluation of the dependence of the barriers upon angular momentum on one hand and upon temperature on the other. It may well be that complex fragment emission will be the most powerful if not the only tool for the characterization of extremely hot nuclei, their free energy and the temperature dependence of the coefficients of its liquid drop-like expansion. As we are writing, the role and scope of intermediate energy nuclear physics is being debated and defined in the experimental and theoretical arenas. If intermediate energy nuclear physics is the physics of hot nuclei near the limit of their (thermal) stability, it is clear already that fission in its generalized aspect of complex fragment emission will be a shining beacon in the golden twilight of nuclei.

Acknowledgements

References

Aichelin J and Hüfner J 1984 *Phys. Lett.* **138B** 15
Alexander J M, Baltzinger C and Gazdik M F 1963 *Phys. Rev.* **129** 1826
Auger G, Jouan D, Plagnol E, Pougheon F, Naulin F, Doubre H and Grégoire C 1985 *Z. Phys.* **A321** 243
Auger F, Berthier B, Cunsolo A, Foti A, Mittig W, Pascaud J M, Plagnol E, Québert J and Wieleczko J P 1987. *Phys. Rev.* **C35** 190
Barwick S W, Price P B, Ravn H L, Hourani E and Hussonnois H 1986 *Phys. Rev.* **C34** 362
Bass R 1974 *Nucl. Phys.* **A231** 45
Bertsch G and Siemens P J 1983 *Phys. Lett.* **126** 9
Bowman D R, Kehoe W L, Charity R J, McMahan M A, Moroni A, Bracco A, Bradley S, Iori I, McDonald R J, Mignerey A C, Moretto L G, Namboodiri M N and Wozniak G J 1987 *Phys. Lett.* **B189** 282
Bowman D R et al 1988 to be published
Businaro U L and Gallone S 1955b *Nuovo Cimento* **1** 1277
Caretto A A, Hudis J and Friedlander G 1958 *Phys. Rev.* **110** 1130
Charity R J, McMahan M A, Bowman D R, Liu Z H, McDonald R J, Wozniak G J, Moretto L G, Bradley S, Kehoe W L, Mignerey A C and Namboodiri M N 1986 *Phys. Rev. Lett.* **56** 1354
Charity R J, Bowman D R, Liu Z H, McDonald R J, McMahan M A, Wozniak G J, Moretto L G, Bradley S, Kehoe W L and Mignerey A C 1988

Nucl. Phys. **A476** 516

Charity R J, McMahan M A, Wozniak G J, McDonald R J, Moretto L G, Sarantites D G, Sobotka L G, Guarino G, Pantaleo A, Fiore L, Gobbi A, and Hildenbrand K D 1988a *Nucl. Phys.* **A483** 371

Charity R J, Colonna N, McMahan M A, Wozniak G J, McDonald R J, Moretto L G, Guarino G, Pantaleo A, Fiore L, Gobbi A, and Hildenbrand K D 1988b to be published

Cohen S, Plasil F and Swiatecki W J 1963 *Proc. Third Conf. on Reactions Between Complex Nuclei*, ed. A. Ghiorso, R. M. Diamond and H. E. Conzett (University of California Press) pp. 325 UCRL-10775

Cohen S, Plasil F and Swiatecki W J 1974 *Ann. Phys.* **82** 557

Ericson T 1960 *Adv. in Phys.* **9** 425

Finn J E, Agarwal S, Bujak A, Chuang J, Gutay L J, Hirsch A S, Minich R W, Porile N T, Scharenberg R P, Stringfellow B C and Turkot F 1982 *Phys. Rev. Lett.* **49** 1321

Fischer M E 1967a *Phys.* **3** 255

Fischer M E 1967b *Rep. Prog. Phys.* **67** Vol. **30** 615

Friedlander G, Miller J M, Wolfgang R, Hudis J and Baker E 1954 *Phys. Rev.* **94** 727

Friedlander G, Friedman L, Gordon B and Yaffe 1963 *Phys. Rev.* **129** 1809

Gales S, Hourani E, Hussonnois M, Schapira J P, Stab L and Vergnes M 1984 *Phys. Rev. Lett.* **53** 759

Gavron, A. 1980 *Phys. Rev.* **C21**, 230.

Han H, Jing K, Plagnol E, Bowman D R, Charity R J, Vinet L, Wozniak G J, and Moretto L G 1988 Lawrence Berkeley Laboratory preprint LBL-25743

MacMurdo K W and Cobble J W 1969 *Phys. Rev.* **182** 1303

McMahan M A, Moretto L G, Padgett M L, Wozniak G J, Sobotka L G and Mustafa M G 1985 *Phys. Rev. Lett.* **54** 1995

Moretto L G, Thompson S G, Routti J and Gatti R C 1972a *Phys. Lett.* **32B** 471

Moretto L G 1972b *Phys. Lett.* **40B** 185

Moretto L G 1975 *Nucl. Phys.* **A247** 211

Moretto L G and Schmitt R P 1976 *J. Phys.* **37C5** 109

Moretto L G and Wozniak G J 1984 *Ann. Rev. Part. Aci.* **34** 189

Nix J R and Swiatecki W J 1965 *Nucl. Phys.* **71** 1

Poenaru D N, Ivascu M, Sandulescu A and Greiner W 1985 *Phys. Rev.* **C32** 572

Price P B, Stevenson J D, Barwick S W and Rarn H L 1985 *Phys. Rev. Lett.* **54** 297

Rose H J and Jones G A 1984 *Nature* **307** 245

Sarantites D G, Bowman D R, Wozniak G J, Charity R J, McDonald R J, McMahan M A, Namboodiri M N and Moretto L G 1987 Lawrence Berkeley Laboratory preprint LBL-24495.

Sauer G, Chandra H and Mosel U 1976 *Nucl. Phys.* **A264** 221

Schröder W U and Huizenga J R 1977 *Ann. Rev. Nucl. Sci.* **27** 465

Shi Y J and Swiatecki W J 1985a *Phys. Rev. Lett.* **54** 300

Shi Y J and Swiatecki W J 1985b *Nucl. Phys.* **A438** 450

Siemens P J 1983 *Nature* **395** 410

Sierk A J 1985 *Phys. Rev. Lett.* **55** 582

Sierk A J 1986 *Phys. Rev.* **C33** 2039

Sobotka L G, Padgett M L, Wozniak G J, Guarino G , Pacheco A J , Moretto L G, Chan Y, Stokstad R G, Tserruya I and Wald S 1983 *Phys. Rev. Lett.* **51** 2187

Sobotka L G, McMahan M A, McDonald R J, Signarbieux C, Wozniak G J, Padgett M L, Gu J H, Liu Z H, Yao Z Q and Moretto L G 1984 *Phys. Rev. Lett.* **53** 2004

Sobotka L G, Sarantites D G, Li Z E, Dines E L, Halbert M L, Hensley D C, Schmitt R P, Majka Z, Nebbia G, Griffin H C and Sierk A J 1987 *Nucl. Phys.* **A471** 131c

Swiatecki W J 1982 *Nucl. Phys.* **A376** 275

Viola V E, Back B B, Wolf K L, Awes T C, Gelbke C K and Breuer H 1982 *Phys. Rev.* **C26** 178

Viola V E, Kwiatkowski K and Walker M 1985 *Phys. Rev.* **C31** 1550

Weisskopf V F 1937 *Phys. Rev.* **52** 295

Weisskopf V F and Ewing D H 1940 *Phys. Rev.* **57** 472

Weisskopf V F 1950 *Phys. Acta* **23** 187

Weisskopf V F 1953 *Arts Sci..* **82** 360

Wheeler J A 1963 *Fast neutron physics part II* (Interscience, New York) pp. 2051

LAWRENCE BERKELEY LABORATORY
TECHNICAL INFORMATION DEPARTMENT
UNIVERSITY OF CALIFORNIA
BERKELEY, CALIFORNIA 94720